

# **Multivariate modeling of metabolic state vulnerabilities across diverse cancer contexts reveals synthetically lethal associations**

Cara Abecunas<sup>1,2,4</sup> and Mohammad Fallahi-Sichani<sup>1,3,5,\*</sup>

<sup>1</sup>Department of Biomedical Engineering, University of Virginia, Charlottesville, VA 22908

<sup>2</sup>Department of Biomedical Engineering, University of Michigan, Ann Arbor, MI 48109

<sup>3</sup>UVA Comprehensive Cancer Center, University of Virginia, Charlottesville, VA 22908

<sup>4</sup>Present address: Vindhya Data Science, 20 Bayless Ridge Court, Morrisville, NC 27560

<sup>5</sup>Lead contact

\*Correspondence: [fallahi@virginia.edu](mailto:fallahi@virginia.edu)

## **Abstract**

Targeting the distinct metabolic needs of tumor cells has recently emerged as a promising strategy for cancer therapy. The heterogeneous, context-dependent nature of cancer cell metabolism, however, poses challenges in identifying effective therapeutic interventions. Here, we utilize various unsupervised and supervised multivariate modeling approaches to systematically pinpoint recurrent metabolic states within hundreds of cancer cell lines, elucidate their association with tissue lineage and growth environments, and uncover vulnerabilities linked to their metabolic states across diverse genetic and tissue contexts. We validate key findings using data from an independent set of cell lines, pharmacological screens, and via single-cell analysis of patient-derived tumors. Our analysis uncovers new synthetically lethal associations between the tumor metabolic state (e.g., oxidative phosphorylation), driver mutations (e.g., loss of tumor suppressor PTEN), and actionable biological targets (e.g., mitochondrial electron transport chain). Investigating these relationships could inform the development of more precise and context-specific, metabolism-targeted cancer therapies.

## **Introduction**

Cancer cells rely on metabolic pathways for a variety of functions, including proliferation, survival, and migration, making metabolism an attractive anti-cancer therapeutic target <sup>1</sup>. Identifying effective metabolic targets for cancer therapy, however, has proven challenging <sup>2</sup>. Tumor cells exhibit a wide range of metabolic states that vary by their tissue of origin, developmental stage, and genetic alterations <sup>3</sup>. They also have remarkable ability to rewire their intracellular metabolic networks in response to diverse environmental cues and changing metabolic demands <sup>4,5</sup>. The context-dependent nature of cancer cell metabolism makes it difficult to identify unique metabolic pathways that are uniformly required for the diverse population of cancer cells across heterogeneous tumors but are not essential for

healthy cells. Despite this challenge, the discovery of novel cancer-specific metabolic dependencies has provided promising opportunities via, for example, targeting genetically mutated enzymes whose upregulated activity is essential for tumor growth <sup>6,7</sup>, or blocking metabolic pathways on which tumor cells with specific oncogenic alterations have developed extraordinarily high dependency <sup>8-10</sup>. Uncovering such context-specific metabolic alterations and dependencies can guide new approaches to target cancer cells.

The search for novel anti-cancer metabolic targets is significantly benefiting from recent developments in characterization of large panels of diverse cancer cell lines, including their genetic dependency maps, genomic, transcriptomic, and metabolomic features <sup>11,12</sup>. Systematic studies have generated and integrated such large-scale datasets to characterize the landscape of metabolic pathway alterations and dependencies across cancer cell lines, demonstrating the context-specific nature of metabolic dependencies, and identifying new metabolic vulnerabilities in cancer cells <sup>13-17</sup>. Building upon promising outcomes from these studies, a critical next step would be to develop computational models that reveal metabolic state-specific gene or pathway co-dependencies to discover potential synthetic lethality imposed by the cancer genotype or tissue context <sup>2</sup>. Because metabolism is heavily dependent on subcellular organelle functions and integrated with processes such as kinase signaling, transcription and chromatin modifications <sup>4,18-21</sup>, it is likely that a multivariate approach may reveal novel co-dependencies among these processes and heterogeneous metabolic states. Importantly, such co-dependencies, which may not be initially apparent, could be exploited to guide the development of new drugs, or repurposing of existing ones, to target cancer cells more precisely.

In this study, we test the hypothesis that genetic, and tissue context-specific therapeutic targets associated with heterogeneous metabolic states in cancer cells could be identified through conditional synthetic lethality. We integrate transcriptomics data from the Cancer Cell Line Encyclopedia, spanning

41 major cancer types, with their mutation profiles and genome-wide DepMap gene dependency scores<sup>12</sup>. We find heterogeneities in some metabolic pathways (such as linoleic acid, phenylalanine, ascorbate and aldarate metabolism) was highly associated with cancer type, while cell line-to-cell line variability in other pathways, such as oxidative phosphorylation (OXPHOS), could not be explained by differences in cancer type or lineage. Furthermore, OXPHOS was the most variable pathway across individual cell lines in at least 11 major cancer types with little association with their growth media composition, suggesting that cell-intrinsic factors drive the majority of OXPHOS heterogeneity in these cell lines. Therefore, we employ multivariate modeling to uncover OXPHOS<sup>High</sup> and OXPHOS<sup>Low</sup> state-specific vulnerabilities in cell lines representing these cancers. Furthermore, we find some specific driver mutations or tissue contexts significantly amplify the impact of OXPHOS state-specific gene dependencies. Loss of PTEN, for example, predicts increased dependency on mitochondrial respiratory chain and enhanced sensitivity to pharmacological inhibitors of mitochondrial ATP synthase in OXPHOS<sup>High</sup> tumor cells. Our approach, therefore, provides a path to identify context-specific, metabolic state-dependent synthetic lethality that could be exploited to guide more precise cancer therapeutic opportunities.

## Results

### Transcriptomics analysis of cancer cell lines reveals cancer type-associated heterogeneities in metabolic pathways

To systematically evaluate metabolic similarities and differences across cell lines representing diverse cancer types, we used RNA sequencing data from the Cancer Cell Line Encyclopedia (CCLE)<sup>22</sup>. By including all cancer types of which 5 CCLE cell lines or more were available, we analyzed 1,341 cell lines spanning 41 major cancer types (Figure 1A). We used uniform manifold approximation and

projection (UMAP) clustering to visualize the degree to which the expression of 1,620 genes representing 85 different metabolic pathways (obtained from the KEGG database<sup>23,24</sup>) varied with cancer type (Figure 1B). The UMAP projection revealed clusters of cell lines that correlated with cancer types based on their metabolic gene expression. Examples of cancers that clustered most distinguishably by UMAP were cell lines representing acute myeloid leukemia, B- and T-lymphoblastic leukemia/lymphoma, diffuse glioma, Ewing sarcoma, Hodgkin and non-Hodgkin lymphomas, neuroblastoma, melanomas, liposarcoma, rhabdoid cancer, and myeloproliferative neoplasms (Figures 1B and S1A). UMAP also revealed patterns of association between cell lines representing distinctive tissue lineages. For example, cell lines of the hematopoietic lineage (including leukemias, lymphomas, and myeloproliferative neoplasms) were all clustered together and separated from non-hematopoietic cell lines (Figure 1B). Clustering of melanoma cell lines of cutaneous and ocular subtype or cell lines of the neuroendocrine lineage (including small cell lung cancer and neuroblastoma) were additional examples, where metabolic gene expression signatures revealed similarities among cancer types with related lineages (Figures 1B and 1C). Interestingly, however, within some cancer types such as non-small cell lung cancer (NSCLC), ovarian epithelial tumor, or esophagogastric adenocarcinoma, we observed substantial differences among individual cell lines (Figures 1C and S1A). In the case of NSCLC, we asked whether these differences might be explained by the NSCLC subtype, including squamous cell carcinoma, adenocarcinoma, and large cell carcinoma. Cancer cell lines representing these subtypes also did not cluster together in the UMAP visualization (Figure S1B), suggesting that other oncogenic events or environmental factors might have a stronger effect on patterns of metabolic gene expression among these cancer cell lines.

Intrigued by the UMAP illustration of possible relationships between the expression of metabolic genes and specific cancer types, we sought to perform a systematic statistical analysis to quantify these

relationships at the level of individual metabolic pathways. To this end, we computed a score representing the activity of each of the 85 metabolic pathways for each cancer type relative to all cancer types using a three-step procedure adapted from Xiao *et al*<sup>25</sup> (see Methods). A metabolic pathway activity score  $<1$  for a cancer type represents reduced pathway activity in that cancer type in comparison with the average pathway activity across all cancer types; scores  $>1$  represent increased activity; and a score of 1 represents activity levels equivalent to the average over all cancer types. Among the 85 KEGG metabolic pathways, 73 exhibited significantly increased or decreased activity in at least one cancer type (Figure 2A). Hierarchical clustering revealed associations between pathway activity scores and each of the 41 cancer types. Cell lines from several haemopoietic cancers (e.g., B- and T-lymphoblastic leukemia/lymphoma, non-Hodgkin lymphoma, acute myeloid leukemia, and myeloproliferative neoplasms) exhibited overall reduced activity in a wide range of metabolic pathways in comparison with most other cancer types (Figures 2A and S2A). The activity of multiple metabolic pathways such as linoleic acid metabolism, metabolism by cytochrome P450, retinol metabolism, ascorbate and aldarate metabolism, and steroid hormone biosynthesis was substantially lower in these hematopoietic cancers relative to most other cancers. The activity of these metabolic pathways, however, were elevated in cell lines of non-small cell lung cancer, lung neuroendocrine tumor, hepatocellular and esophageal squamous cell carcinomas (Figure 2A).

To identify those metabolic pathways that varied most profoundly with cancer type, we performed principal component analysis (PCA) on pathway activity scores across 41 cancer types. The first eight principal components (PCs) captured  $>80\%$  of the overall variance in data (Figure S2B). To quantify the relative impact of each pathway on data variance in the principal component space, we computed the absolute sum of PCA loadings for each pathway over the first eight PCs. Among the top 10 variable pathways across all cancer types were pathways involved in lipid, amino acid, and vitamin

metabolism, such as linoleic acid, phenylalanine and histidine metabolism, steroid hormone, and glycosphingolipid biosynthesis, and ascorbate and aldarate metabolism (Figures 2B and S2C). On the other hand, the pathways with the least amount of overall variability across different cancer types were energy-producing and carbohydrate metabolism pathways, such as oxidative phosphorylation (OXPHOS), citrate (TCA) cycle, pentose phosphate pathway, and N-glycan biosynthesis (Figures 2B and S2C). Together, our systematic analysis of metabolic gene expression data across cell lines showed substantial cancer type-associated heterogeneities in some metabolic pathways (such as linoleic acid and ascorbate metabolism), while variability in some other pathways, such as OXPHOS, could not be explained by differences in cancer type.

### **OXPHOS state exhibits substantial cell line-to-cell line heterogeneity independent of cancer type**

Focusing on each cancer type separately, we then sought to assess the extent of heterogeneity in each metabolic pathway among individual cell lines. To identify heterogeneous metabolic pathways in cell lines within each cancer type, we first performed PCA on the gene expression dataset from cell lines of that cancer type. We computed metabolic gene variability scores as the absolute sum of the PCA loading values across the top PCs accounting for at least 80% of the variance in each dataset. We then applied pre-ranked gene set enrichment analysis (GSEA) to the ranked lists of metabolic gene variability scores. GSEA revealed cell lines of the same cancer type with significant variability in genes found in 25 metabolic pathways (Figure 3A). Hierarchical clustering revealed several cancer types exhibiting more profound cell line-to-cell line heterogeneity in some pathways than others. We thus ranked metabolic pathways according to the number of cancer types showing significant cell line-to-cell line heterogeneity (Figure 3B). The top three pathways with the highest level of cell line-to-cell line heterogeneity were retinol metabolism, cytochrome P450 metabolism, and oxidative phosphorylation (OXPHOS). The first

two were also among the pathways whose relative activity varied substantially from one cancer type to another (Figures 2A and S2C). Surprisingly, however, OXPHOS had shown the least amount of variability among cell lines when compared collectively across distinct cancer types (Figures 2A and 2B). Other metabolic pathways showed different trends; ascorbate and aldarate metabolism, for example, was largely variable across diverse cancer types as well as among individual cell lines of some cancer types (Figures 2A, S2C and 3A). These distinct patterns were also clear when we visualized the distributions of the mean and interquartile range (IQR) values for the cumulative abundance of gene transcripts corresponding to each metabolic pathway (Figures 3C and S3). For example, the median and IQR for the abundance of ascorbate and aldarate metabolism transcripts varied largely (up to 7-fold and 21-fold, respectively) among groups of myeloproliferative neoplasm, AML, melanoma, colorectal adenocarcinoma, and pancreatic adenocarcinoma cell lines. In contrast, the mean and IQR for the abundance of OXPHOS transcripts varied minimally (<1.5-fold and <1.3-fold, respectively) across the same groups of cell lines (Figures 3C).

Cancer cell lines are grown in different culture media that influence their metabolic state and their dependencies<sup>13,14,26</sup>. We thus quantified the statistical contribution of growth media composition toward the observed cell line-to-cell line heterogeneity in metabolic pathways. We used the same approach as described above to compute relative metabolic pathway activity scores for cell lines grouped based on their growth media compositions (Figure 4A). Hierarchical clustering and PCA analysis revealed subsets of metabolic pathways with activities that were associated most or least with each of the 21 chemically distinct media compositions (Figures 4A, 4B and S4). The top two pathways whose activity was most significantly associated with growth media were linoleic acid metabolism and ascorbate and aldarate metabolism (Figure 4B). This observation suggests that the high level of variability in these pathways across cancer types and individual cell lines could be also influenced by

differences in extrinsic factors in their growth environment. Interestingly, however, variations in a subset of pathways, including OXPHOS, TCA cycle, pentose phosphate pathway and thiamine metabolism exhibited little association with growth media composition (Figure 4B). Although these results do not rule out the impact of growth media composition on OXPHOS pathway, they suggest a dominant role for cell-intrinsic factors in driving the observed cell line-to-cell line heterogeneity in these pathways among the tested cell lines.

### **Multivariate modeling uncovers pan-cancer gene vulnerabilities associated with OXPHOS state**

As shown above, OXPHOS was among the most variable pathways across individual cell lines in at least 11 out of 41 major cancer types and such variability could not be explained solely by differences in growth media composition. Therefore, we set out to leverage such heterogeneity to uncover OXPHOS state-associated gene vulnerabilities in these cancers. We hypothesized that novel therapeutic targets specific to OXPHOS<sup>High</sup> and OXPHOS<sup>Low</sup> states could be identified through conditional synthetic lethality. To test this hypothesis, we analyzed the data from genome-wide DepMap CRISPR knockout screen across 495 CCLE cell lines<sup>12</sup>, representing 11 cancer types with significant levels of cell line-to-cell line heterogeneity in OXPHOS, including non-small cell lung cancer (NSCLC), invasive breast carcinoma (IBC), diffuse glioma (DG), head and neck squamous cell carcinoma (HNSCC), melanoma, cervical adenocarcinoma (CAC), ovarian epithelial tumor (OET), pancreatic adenocarcinoma (PAC), breast ductal carcinoma in situ (BDCIS), colorectal adenocarcinoma (CRAC), and renal cell carcinoma (RCC). We used DepMap gene dependency scores as measures of the effect of 17,202 gene knockouts on viability of each cell line, where a score of 0 indicates no inhibitory effect (corresponding to a non-essential gene), and 1 indicates complete inhibitory effect (corresponding to an essential gene)<sup>27</sup>. To systematically identify gene vulnerabilities that were most strongly related to OXPHOS state, we

performed feature selection and multivariate modeling.

We first calculated OXPPOS state scores across the cell lines, defined as the average of Z scores for the expression levels of 113 OXPPOS genes. To amplify the impact of OXPPOS<sup>High</sup> and OXPPOS<sup>Low</sup> groups of cell lines in feature selection, we ordered cell lines based on their OXPPOS state scores and included only the top and bottom 33 percentiles, resulting in 328 cell lines (Figure S5A). As the first step of feature selection, we removed genes with dependency scores that varied minimally across OXPPOS<sup>High</sup> and OXPPOS<sup>Low</sup> cell lines, narrowing down the list of genes to 3,624 (Figure S5B). We then used elastic net regularization to select a subset of the remaining genes based on their association with the OXPPOS state score. We optimized the parameters of elastic net model and trained it over 150 iterations (using 10-fold cross validation) using a randomly selected group of 296 cell lines out of 328 cell lines, leaving the other 32 cell lines to be used as a test set for independent validation (Figures S5C and S5D). 200 genes appeared in at least 50% of all elastic net iterations (Figure S5E). We imported these genes into Enrichr to search for potential enrichment of cellular components, biological processes, and pathways associated with the selected gene vulnerabilities (Figures 5A and S5F). We found OXPPOS<sup>High</sup> cell lines were vulnerable to gene knockouts associated with mitochondrial membrane, respiratory electron transport chain and histone acetyl transferase complexes. OXPPOS<sup>Low</sup> cell lines, on the other hand, were vulnerable to knockouts associated with Rho GTPase signaling, focal adhesion, cell-matrix junctions, lysosomes, and the trans-Golgi network.

To quantify the relative importance of 200 gene dependencies in predicting the OXPPOS state of each cell line, we built a partial least-square regression (PLSR) model<sup>28,29</sup>. The overall performance of the PLSR model was evaluated based on the percentage of variance in OXPPOS state scores explained ( $R^2$ ) or predicted ( $Q^2$ ) by the variance in gene dependency scores (Figure 5B). The model revealed high performance with  $R^2$  of 81.9% and  $Q^2$  of 63.3% (using leave-one-out cross-validation) for the first four

PLS components. To further evaluate the model performance, we correlated the true OXPHOS state scores and the state scores predicted (based on leave-one-out) by the PLSR model, which led to a Pearson's correlation coefficient of 0.9 ( $P = 4.8 \times 10^{-111}$ ) across 296 cell lines (Figure 5C; left panel). To independently validate the model, we used the test set of 32 CCLE cell lines that were not included in either elastic net regularization or PLSR training steps (Figure S5C). The trained PLSR model was able to predict OXPHOS state scores in the test set with a Pearson's correlation coefficient of 0.49 ( $P = 0.004$ ) (Figure 5C; right panel).

The high performance of the PLSR model suggests that variations in the knockout effects of predictive genes can explain variability in OXPHOS state across heterogeneous cell lines. This was also evident from the observation that cell lines with high or low OXPHOS scores could be efficiently separated based on their PLSR scores along PLS1 to PLS4 (Figure 5D). To identify those gene vulnerabilities that most significantly predicted the OXPHOS state, we calculated the variable importance in projection (VIP) scores along the first four PLS components. We identified 64 genes showing VIP scores of greater than one (Figure S5G). We then used a combination of permutation testing and Pearson's correlation analysis to identify 53 out of 64 genes, which not only showed significant differences in their dependencies between subgroups of OXPHOS<sup>High</sup> and OXPHOS<sup>Low</sup> cell lines ( $P \leq 0.05$ ), but also retained their correlations with OXPHOS state score when evaluated across the complete list of 495 cell lines ( $FDR \leq 0.05$ ). Among these genes, we focused on those whose median dependencies between subgroups of OXPHOS<sup>High</sup> and OXPHOS<sup>Low</sup> cell lines were larger than 0.15. This led to a final list of 12 gene vulnerabilities strongly associated with the OXPHOS<sup>High</sup> state and 15 gene vulnerabilities strongly associated with the OXPHOS<sup>Low</sup> state (Figure 5E).

Among the most significant predictors of OXPHOS<sup>High</sup> state were gene dependencies associated with mitochondrial membrane and function, including MICOS10 and TFAZZIN (which play critical

roles in maintaining mitochondrial inner membrane structure and function), COQ4, NDUFB8, NDUFS1 and NDUF2 (mediators of mitochondrial membrane respiratory chain), DNMI1 (a mediator of mitochondrial fission), and MRPL58 (a component of the large mitochondrial ribosome required for mitochondrial gene translation). We also found EP300 (a histone acetyltransferase that regulates transcription via chromatin remodeling) and COASY (an enzyme involved in biosynthesis of coenzyme A, a carrier of acetyl and acyl groups) to be additional OXPHOS<sup>High</sup> state-specific dependencies. On the other hand, the list of OXPHOS<sup>Low</sup> state-specific dependencies included ENO1 (a key glycolytic enzyme), TIPARP (a regulator of glycolytic gene expression through HIF-1 $\alpha$ <sup>30</sup>), and genes involved in Rho and Rab GTPase signaling, such as ARHGEF7, NCKAP1 and MYH9 (involved in cytoskeleton regulation), RAB6A, SNAP23 and EFR3A (involved in vesicular trafficking, membrane fusion and Golgi organization).

### **Statistical analysis reveals synthetically lethal associations between OXPHOS state, driver mutations and tissue context**

Next, we asked whether any of the OXPHOS state-associated gene vulnerabilities were enriched more significantly in cell lines originating from specific tissue types or those carrying specific driver mutations. To answer this question, we compared median gene dependency between OXPHOS<sup>High</sup> and OXPHOS<sup>Low</sup> subgroups among cell lines grouped based on cancer type or occurrence of the top 25 commonly mutated driver genes<sup>31</sup> (Figure S6A). Among these genes, we focused on the top eleven, which carried mutations in at least 15 tested cell lines, including TP53, KRAS, PIK3CA, BRAF, APC, ARID1A, PTEN, NF1, FAT1, KMT2D, CREBBP (Figure S6B). To assess the statistical significance of the observed differences in gene dependency, we performed permutation testing by randomly shuffling the OXPHOS state labels (High and Low) across cell lines participating in each comparison and

computing permutation  $P$  values. We then used  $P \leq 0.01$  as the significance cutoff to identify mutations and tissue types associated with enhanced OXPPOS state-specific gene dependencies relative to pan-cancer analysis (Figures 6, S6C and S6D).

Focusing on OXPPOS<sup>High</sup> state-specific dependencies, we found that mutations in the tumor suppressor PTEN were consistently associated with significant increases in dependency on genes involved in mitochondrial membrane respiratory chain, including COQ4, NDUFB8, NDUFS1 and NDUFC2 (Figures 6A and 6B). KRAS and APC mutations were associated with enhanced dependency on DNMT1L (Figure S6C), and the effect of EP300 gene knockout in OXPPOS<sup>High</sup> cell lines was significantly greater in the presence of mutations in chromatin regulators KMT2D or ARID1A (Figure 6C). We also identified cases, where an OXPPOS<sup>High</sup> state-specific gene dependency was enriched in cell lines from a specific cancer type, such as EP300 dependency in melanoma and ovarian epithelial tumor cell lines and MRPL58 dependency in invasive breast carcinoma and head and neck squamous cell carcinoma lines (Figures 6A and 6C). Focusing on OXPPOS<sup>Low</sup> state-specific dependencies, we found that multiple gene dependencies associated with cytoskeleton regulation and vesicle trafficking (such as ARHGEF7, RAB6A, NCKAP1) were significantly enriched in pancreatic adenocarcinoma cell lines (Figure 6D). The most frequent oncogenic events correlated with OXPPOS<sup>Low</sup> state-specific gene dependencies were FAT1 mutations that were associated with enhanced dependency on ARHGEF7, ENO1 and ZFP36L1, and ARID1A mutations that were associated with increased dependency on RAB6A, RRAGC, TIPARP and ZFP36L1 (Figures 6D and S6D).

Together, these results suggest that synthetically lethal relationships exist between the tumor metabolic state, driver mutations and specific genes or pathways that could be potentially exploited to selectively target cancer state-specific vulnerabilities. To further explore this idea, we focused our attention on PTEN mutations based on their profound association with OXPPOS<sup>High</sup> state-specific

dependencies on mitochondrial membrane structure and electron transport chain.

## **Loss of PTEN predicts increased dependency on mitochondrial respiratory chain in OXPHOS<sup>High</sup> tumor cells**

To independently test the impact of damaging mutations in PTEN on OXPHOS state-specific dependencies, we used the Cancer Therapeutics Response Portal (CTRP) data to analyze the sensitivity of 799 genetically characterized cancer cell lines to 545 small-molecule probes and drugs<sup>32</sup>. We used transcriptomics data to define groups of OXPHOS<sup>Low</sup> and OXPHOS<sup>High</sup> cell lines based on whether their OXPHOS state scores were ranked within the top or bottom 33 percentiles. We then compared the median sensitivity of OXPHOS<sup>Low</sup> and OXPHOS<sup>High</sup> cell lines to each tested small molecule based on the area of the dose-response curve (AUC) measurements. Within the OXPHOS<sup>High</sup> group, we also compared the median sensitivity of PTEN-wildtype (PTEN<sup>WT</sup>) and PTEN-mutated (PTEN<sup>Mut</sup>) subgroups. Among all small molecules tested, we found oligomycin A, a well-known inhibitor of mitochondrial ATP synthase<sup>33</sup>, to exhibit the strongest differential effect on OXPHOS<sup>High</sup> cell lines relative to OXPHOS<sup>Low</sup> cell lines (Median difference = 0.9;  $P = 0.04$ ), while being more effective in the PTEN<sup>Mut</sup> subgroup than in PTEN<sup>WT</sup> cells (Median difference = 1.7;  $P = 0.07$ ) (Figure 7A). Although not statistically significant, neopeltolide, a natural product which was recently discovered as an inhibitor of mitochondrial ATP synthesis<sup>34</sup>, was also among the top 4 compounds with increased median efficacy in OXPHOS<sup>High</sup> cell lines compared with OXPHOS<sup>Low</sup> cell lines (Median difference = 0.9), while also being more effective in the PTEN<sup>Mut</sup> subgroup than in PTEN<sup>WT</sup> cells (Median difference = 0.9). These results are consistent with the evidence from the CRISPR knockout screen data, showing enhanced dependency of PTEN<sup>Mut</sup>/OXPHOS<sup>High</sup> tumor lines on mitochondrial electron transport chain.

To further explore the clinical relevance of the role of PTEN loss in tumor cells' dependency on

mitochondrial electron transport chain, we turned our focus on diffuse gliomas, the most common malignant adult brain cancer, in which genetic loss of PTEN expression is frequently observed<sup>35</sup>. Multiple studies have reported the sensitivity of glioma cell lines and tumors to OXPHOS inhibitors that block mitochondrial electron transport chain protein complexes *in vitro* and *in vivo*<sup>36–38</sup>. However, little is known about how the genetic background of glioma tumors might influence such metabolic dependency. To explore this, we analyzed DNA- and RNA-sequencing data and matched clinical annotation for glioma patients across glioma subtypes assembled by the GLASS consortium<sup>39</sup>. Tumors from 64 out of 222 patients (i.e., ~29% of patients) carried PTEN mutations, including truncating, missense, in-frame, and splice-site mutations. The presence of such mutations in tumors were associated with significantly shorter overall survival in glioma patients (Figure 7B). To infer how PTEN expression might be associated with glioma tumor state, we performed transcriptome-wide co-expression analysis across 79 tumor samples for which RNA-sequencing data were available. We used Spearman's correlation analysis to rank transcripts based on the association of their abundance with PTEN expression (Figure S7A). We then imported the list of 571 transcripts that significantly and negatively correlated with PTEN expression (Spearman's  $r < 0$ ;  $FDR \leq 0.05$ ) into Enrichr to identify cellular components and biological processes associated uniquely with loss of PTEN. The most significantly enriched components and biological processes were mitochondrial membrane, mitochondrial respiratory chain complex, proton-transporting ATP synthase complex and cellular respiration (Figures 7C, S7B, S7C and S7D). These results suggest that glioma tumors with loss of PTEN expression exhibit a higher expression of components of the mitochondrial electron transport chain and ATP synthase complex.

To further test the association of PTEN loss with mitochondrial electron transport chain components at a single-cell level, we analyzed single-cell RNA-sequencing data of genetically profiled patient-derived glioblastoma tumors, including 10,268 PTEN<sup>Mut</sup> malignant cells isolated from a group of

6 patients and 23,229 PTEN<sup>WT</sup> tumor cells from a group of 20 patients<sup>40</sup>. We then compared the abundance of transcripts representing individual components of the electron transport chain, including Complex I-IV and ATP synthase, between PTEN<sup>Mut</sup> and PTEN<sup>WT</sup> cells. We observed significantly higher expression levels for Complex I, III, IV and ATP synthase genes among PTEN<sup>Mut</sup> cells and a lower level of cell-to-cell variability in their expression (as evaluated by IQR) in comparison with PTEN<sup>WT</sup> cells (Figure 7D). Together, these results reveal a notable upward shift in the expression of mitochondrial respiratory chain complex genes among PTEN<sup>Mut</sup> glioma cells, that is consistent with their enhanced dependency on electron transport chain in comparison with PTEN<sup>WT</sup> tumor cells.

## Discussion

In this paper, we used a combination of unsupervised and supervised multivariate analysis approaches to integrate transcriptomics data from hundreds of cancer cell lines with their gene dependency scores and mutation profiles, and thereby predict metabolic state-specific vulnerabilities across various tumor lineages and common oncogenic contexts. Our systematic analysis complements previous studies<sup>11,13,15,16</sup> by revealing the extent to which heterogeneity in diverse metabolic pathways across cancer cell lines can be explained by differences in their growth environment, their tissue of origin and developmental lineage, or potentially other cell-intrinsic mechanisms. Furthermore, we uncover synthetically lethal associations between the cancer cells' metabolic state, their driver mutations, and potentially actionable biological targets, that could guide future studies toward more precise and context-specific therapeutic opportunities.

We used transcriptomics data to infer the activity of metabolic pathways across more than a thousand cell lines without directly accounting for metabolic changes at the flux level or abundance of metabolites. Despite this limitation, we were able to capture key variations in inferred metabolic

pathway activities that were consistent with those derived from metabolomics studies of cell lines grown in identical conditions. For example, our analysis highlighted previously reported metabolic differences between hematopoietic and non-hematopoietic cancers as well as other metabolic variations associated with cancer types<sup>11,15,16</sup>. We also unmasked metabolic similarities among cell lines derived from cancers with related development lineage but in distinct anatomic positions. For example, cell lines of the lung neuroendocrine lineage (represented mostly by the small cell lung cancer cell lines) metabolically clustered more closely with neuroblastoma cell lines rather than with non-small cell lung cancer lines; esophageal squamous cell carcinoma lines also clustered with head and neck squamous cell carcinoma lines rather than with esophagogastric adenocarcinoma lines; and melanoma cell lines of cutaneous and ocular type clustered together. These examples are consistent with previous reports indicating strong associations between metabolic programs and epigenetically regulated tissue lineage and differentiation programs<sup>15,41</sup>, and highlight the need for integrative multi-omics approaches to build a comprehensive picture of tumor metabolism<sup>19</sup>.

Consistent with data from the metabolomics studies<sup>15</sup>, we also observed that pathways associated with lipid, amino acid and carbohydrate metabolism as well as mitochondrial pathways such as OXPHOS accounted for the majority of metabolic heterogeneity among cancer cell lines. For many of these pathways, the observed heterogeneity was highly associated with either cancer type and/or growth media. However, cell line-to-cell line heterogeneity in OXPHOS appeared to be mostly independent of cancer type. Focusing on cancer cell lines within each cancer type separately, we found OXPHOS was highly variable across individual cell lines in at least 11 major cancer types with little association with growth media composition. We found that the OXPHOS state in these cell lines was associated with significant and reproducible gene dependencies. Major OXPHOS<sup>Low</sup> state-specific dependencies included genes involved in cytoskeleton regulation, vesicular trafficking, Golgi organization and

membrane fusion. These results show that alterations in cellular energy status could influence tumor cell dependency on the function of other subcellular organelles such as the Golgi apparatus, and support the idea to target such organelles as potentially selective vulnerabilities associated with tumor metabolic state<sup>18</sup>. On the other hand, OXPHOS<sup>High</sup> state-specific vulnerabilities included genes encoding enzymes that mediate the mitochondrial membrane respiratory chain and ATP synthesis, as well as genes with key roles in the control and maintenance of mitochondrial shape, crista junctions, and architecture. These findings are consistent with various evidences, indicating a tight connection between mitochondrial network structure and bioenergetics<sup>21,42,43</sup>, and suggest that mitochondrial network dynamics are linked to metabolic state-specific therapeutic vulnerabilities<sup>44</sup>.

Finally, our analysis revealed that OXPHOS state-specific gene dependencies were enhanced in the presence of some common driver mutations or in specific tissue lineages. We found, for example, that loss of tumor suppressor PTEN was associated with the increased dependency of OXPHOS<sup>High</sup> tumor cells on mitochondrial respiratory chain and their enhanced sensitivity to pharmacological inhibitors of mitochondrial ATP synthase. This finding is also supported by a previous report pointing to increased sensitivity of PTEN-deficient fibroblasts to inhibition of mitochondrial complex I in comparison with PTEN-wildtype cells<sup>45</sup>. These observations may be especially significant given the narrow therapeutic index of recently developed complex I inhibitors such as IACS-010759 in clinical trials<sup>46,47</sup>, and highlight the importance of identifying specific subsets of patients that may actually benefit from such therapies despite the side effects. Importantly, loss of PTEN mutations are prevalent and predict poor survival in multiple cancers, including gliomas<sup>39</sup>. Our transcriptomics analysis of patient-derived glioma tumors revealed a strong association between loss of PTEN and increased expression of genes encoding mitochondrial electron transport chain. These findings are consistent with a recent discovery of a glioma subtype signified by a substantial increase in OXPHOS and

mitochondrial function and enhanced sensitivity to inhibitors of mitochondrial protein translation and electron transport chain<sup>48</sup>. Multiple reports have demonstrated the increased efficacy of these inhibitors against high-grade glioma tumors both *in vitro* and *in vivo*<sup>36–38,49</sup>, providing a promising path toward their clinical evaluation individually or in combination therapies<sup>50</sup>. For example, an ongoing phase II trial is testing the efficacy of mitochondrial complex I inhibitor metformin in combination with temozolomide and radiotherapy in patients with tumors that express an OXPHOS<sup>High</sup> signature at diagnosis (NCT04945148). Findings from our study may inform this trial and other clinical studies of mitochondrial inhibitors (e.g., NCT02780024, NCT05929495, NCT05183204, NCT05824559) by proposing that PTEN loss, in addition to the tumor OXPHOS state, may serve as a predictor of therapeutic response. Future studies may also leverage these findings to elucidate the mechanistic basis of the identified synthetically lethal associations and further evaluate their clinical relevance and therapeutic potential in the presence of key microenvironmental players of tumor metabolism.

## Methods

### Transcriptomic analysis and visualization of metabolic heterogeneity in cancer cell lines

To systematically evaluate metabolic similarities and differences across cell lines representing diverse cancer types, we used RNA sequencing data from the Cancer Cell Line Encyclopedia (23Q2 release). Cancer types were selected if 5 or more cell lines were RNA-sequenced, resulting in 1,341 cell lines spanning across 41 cancer types. Log<sub>2</sub>-transformed gene expression data (i.e., log<sub>2</sub>(TPM+1)) was z-scored for all unique KEGG metabolic genes (1,620 genes in 85 metabolic pathways<sup>25</sup>) across all cell lines. Uniform manifold approximation and projection (UMAP) clustering was performed in R using the *umap* package (0.2.10.0) with z-scored data using the following parameters: nearest neighbor (*n\_neighbors*) = 50, minimum distance (*min\_dist*) = 0.5, and distance metric (*metric*) = Pearson.

## Calculation of pathway activity scores across different cancer types (or growth media)

We computed a score representing the activity of each of the 85 metabolic pathways for each of the cancer types (or growth media) relative to all cancer types (or all growth media) using a three-step procedure adapted from Xiao *et al*<sup>25</sup>. In the first step, we calculated the mean expression level ( $E_{i,j}$ ) for each of the 1,620 metabolic genes (i.e., the  $i$ -th metabolic gene) across cell lines within each of the 41 cancer types (i.e., the  $j$ -th cancer type) or each of the 21 distinct growth medium compositions (i.e., the  $j$ -th growth medium):

$$E_{i,j} = \frac{\sum_{k=1}^{n_j} g_{i,k}}{n_j} \quad (1)$$

, where  $n_j$  is the number of cell lines associated with the  $j$ -th cancer type (or the  $j$ -th growth medium type), and  $g_{i,k}$  is the  $\log_2(\text{TPM}+1)$  expression level of the  $i$ -th gene in the  $k$ -th cell line in this cancer type (or medium type). In the second step, the relative gene expression level of the  $i$ -th gene in the  $j$ -th cancer type (or the  $j$ -th medium type) or  $r_{i,j}$  was calculated as the ratio of  $E_{i,j}$  to its average over all cancer types (or all medium types):

$$r_{i,j} = \frac{E_{i,j}}{\frac{1}{N} \sum_j^N E_{i,j}} \quad (2)$$

, where  $N$  is the number of cancer types (i.e., 41) or medium types (i.e., 21).  $r_{i,j}$  values above 1 indicates that the expression level of gene  $i$  is higher in cancer type  $j$  (or medium type  $j$ ) compared to the average expression level over all cancer types (or all medium types). In the third step, pathway activity score ( $p_{t,j}$ ) for the  $t$ -th pathway and the  $j$ -th cancer type (or the  $j$ -th medium type) was calculated as the weighted average of  $r_{i,j}$  over all genes included in the pathway:

$$p_{t,j} = \frac{\sum_{i=1}^{m_t} w_i \times r_{i,j}}{\sum_{i=1}^{m_t} w_i} \quad (3)$$

, where  $m_t$  is the number of genes in pathway  $t$ , and  $w_i$  is a weight factor equal to the reciprocal of the

number of pathways that include the  $i$ -th gene. To avoid pathway activity scores being affected by genes with low and high expression levels, we removed outliers in each pathway defined by genes with expression levels  $< 0.001$  and genes with relative expression levels greater than  $3 \times 75^{\text{th}}$  percentile or below  $1/3 \times 25^{\text{th}}$  percentile. We calculated activity scores for pathways that had at least 5 genes after filtering. Statistical significance of lower or higher pathway activity in a certain cancer type (or medium type) was evaluated by a random permutation test. Cancer type labels (or media culture labels) were randomly shuffled 5,000 times to simulate a null distribution of the pathway activity scores. We then statistically compared the shuffled pathway activity scores to the original, non-shuffled dataset and computed an empirical  $P$  value defined as the fraction of random pathway activity scores larger than  $p_{t,j}$  (if  $p_{t,j} > 1$ ) or smaller than  $p_{t,j}$  (if  $p_{t,j} < 1$ ) to determine if activity of a pathway is significantly higher or lower in a cancer type (or medium type) than average. If a pathway activity was insignificant (i.e.,  $P > 0.05$ ), the activity score was assigned a value of 1. For the analysis of growth media, only those associated with at least 10 cell lines were used.

To determine the least and most variable metabolic pathways across cancer types or growth media, we performed principal component analysis (PCA) on pathway activity scores using the *prcomp* built-in R function. For each metabolic pathway, we calculated the sum of the absolute value of the loadings in the top 8 PCs (for cancer type analysis) or the top 4 PCs (for media type analysis) as they accounted for at least 80% of the variance in data.

### **Analyzing cell line-to-cell line heterogeneity in metabolic pathways**

To determine the extent of cell line-to-cell line heterogeneity in each cancer types, we used a three-step procedure adapted from Xiao *et al*<sup>25</sup>. First, we performed PCA on  $z$ -scored metabolic gene expression data within each cancer type. We computed metabolic gene variability scores as the absolute sum of the

PCA loading values across the top PCs accounting for at least 80% of the variance in data. To identify which metabolic pathways were most variable across cell lines within each cancer type, we applied pre-ranked gene set enrichment analysis (GSEA) to the ranked lists of metabolic gene variability scores. Scores were ranked in descending order and ran in pre-rank GSEA using the *fgseaSimple* function in the *fgsea* package in R (1.20.0). GSEA was performed against the same 85 KEGG metabolic pathways. A cancer type was determined to be significantly heterogeneous for a metabolic pathway if the GSEA generated  $FDR \leq 0.05$ . If a cancer type was significantly heterogeneous for a specific metabolic pathway, we calculated metabolic state scores (e.g., OXPHOS state scores) across the cell lines within the cancer type. Metabolic state scores were calculated as mean z-score values across the genes found within the specific metabolic pathway.

### **Feature selection and multivariate modeling to reveal gene dependencies associated with OXPHOS state**

To systematically identify gene vulnerabilities associated with OXPHOS state, we performed feature selection and multivariate modeling using DepMap gene dependency scores, representing the effect of genome-wide knockout effects on cell viability. A dependency score of 0 indicates no inhibitory effect (corresponding to a non-essential gene), and 1 indicates complete inhibitory effect (corresponding to an essential gene)<sup>27</sup>. We first calculated OXPHOS state scores across the cell lines, defined as the average of z-scores for the expression levels of 113 OXPHOS genes. To amplify the impact of OXPHOS<sup>High</sup> and OXPHOS<sup>Low</sup> groups of cell lines in feature selection, we ordered cell lines based on their OXPHOS state scores and included only the top and bottom 33 percentiles, resulting in 328 cell lines. As the first step of feature selection, we removed genes with dependency scores that varied minimally across OXPHOS<sup>High</sup> and OXPHOS<sup>Low</sup> cell lines. To this end, gene dependency score interquartile range (IQR)

values were calculated across cell lines and genes with  $IQR < 0.09$  were removed, narrowing down the list of genes from 17,202 to 3,624. We then used elastic net regularization, which integrates the penalty functions of least absolute shrinkage and selection operator (LASSO; L1 penalty) and ridge regression (L2 penalty), to further reduce the number of features and select a subset of the remaining genes based on their association with the OXPPOS state score. Elastic net was run in R using the *cv.glmnet* function in the *glmnet* package (4.1-7). We first optimized the alpha ( $\alpha$ ), the parameter that controls the weight of L1 and L2 penalties, across the 296 cell lines in the training dataset. We held out a random set of 32 cell lines with variable OXPPOS state scores as the test dataset for independent validation. 150 elastic net iterations (using 10-fold cross validation) were run with  $\alpha$  ranging from 0.1 to 0.9 for a total of 1,350 models. We reported the smallest mean squared error (MSE) associated with each model based on the minimum lambda (*lambda.min* or  $\lambda_{\min}$ ). Optimized elastic net  $\alpha$  was determined based on the smallest reported median MSE. We selected genes that appeared in at least 50% of the 150 optimized elastic net iterations. The list of 200 selected genes with positive and negative mean coefficients were used in Enrichr (<https://maayanlab.cloud/Enrichr/>)<sup>51</sup> to determine pathways and cellular components associated with OXPPOS<sup>High</sup> and OXPPOS<sup>Low</sup> state dependencies, respectively.

To quantify the relative importance of 200 gene dependencies in predicting the OXPPOS state of each cell line, we built a partial least-square regression (PLSR) model<sup>28,29</sup> using the built-in MATLAB function *plsregress*. To evaluate the predictability of the linear relationship between the input (i.e., gene dependency values) and output variables (i.e., OXPPOS state scores), we used leave-one-out cross-validation. The goodness of fit for each model was calculated using  $R^2$ . Prediction accuracy was evaluated by  $Q^2$  and pairwise Pearson's correlations between the measured and predicted OXPPOS state scores. To independently validate the model, we also used the test set of 32 cell lines that were not included in either elastic net regularization or PLSR training steps. For the assessment of relative

variable importance in the PLSR model, the information content of each variable was assessed by its variable importance in the projection (VIP) score<sup>52</sup>. Based on  $|VIP| \geq 1$ , we identified 64 genes whose dependency scores appeared to be the most significant predictors of the OXPHOS state.

To further narrow down the list of genes (based on significance) for the next steps of analysis, we used a combination of correlation and permutation testing. OXPHOS state scores for all 495 cell lines were correlated with their associated gene dependency scores for each of the 64 genes using Pearson's correlation (R built-in function *cor.test*). Correlation *P* values were adjusted by calculating FDR values using R's built-in function *p.adjust*. In the permutation test, we assessed the gene knockout effect in OXPHOS<sup>High</sup> versus OXPHOS<sup>Low</sup> cell lines (164 cell lines per group) by calculating the difference between the states' median gene dependency scores. A positive difference indicates OXPHOS<sup>High</sup> cell lines are more sensitive to the gene knockout (i.e., OXPHOS<sup>High</sup> vulnerability) while a negative difference indicates OXPHOS<sup>Low</sup> cell lines are more sensitive to the gene knockout (i.e., OXPHOS<sup>Low</sup> vulnerability). Statistical significance of gene knockout effect was evaluated by a random permutation test. OXPHOS states (i.e., OXPHOS<sup>High</sup>, OXPHOS<sup>Low</sup>) were randomly shuffled 8,000 times to simulate a null distribution of the differences between the states' median gene dependency. We then statistically compared the shuffled differences to the original, non-shuffled dataset and computed an empirical *P* value to determine if gene knockout effect is a significant OXPHOS<sup>High</sup> or OXPHOS<sup>Low</sup> vulnerability. The overlap between correlation and permutation analyses found 53/64 gene knockouts to be significant ( $P \leq 0.05$  for permutation test and  $FDR \leq 0.05$  for Pearson correlation). Among these genes, we focused on those whose median dependencies between subgroups of OXPHOS<sup>High</sup> and OXPHOS<sup>Low</sup> cell lines were larger than 0.15. This led to a final list of 12 gene vulnerabilities strongly associated with the OXPHOS<sup>High</sup> state and 15 gene vulnerabilities strongly associated with the OXPHOS<sup>Low</sup> state.

## **Analysis of statistical associations between OXPPOS state, driver mutations and tissue context**

To determine whether any of the OXPPOS state-associated gene vulnerabilities were enriched more significantly in cell lines originating from specific tissue types or those carrying specific driver mutations, we compared median gene dependency between OXPPOS<sup>High</sup> and OXPPOS<sup>Low</sup> subgroups among cell lines grouped based on cancer type or occurrence of the top 25 commonly mutated driver genes<sup>31</sup>. Among these genes, we focused on the top eleven, which carried mutations in at least 15 tested cell lines, including TP53, KRAS, PIK3CA, BRAF, APF, ARID1A, PTEN, NF1, FAT1, KMT2D, CREBBP. To assess the statistical significance of the observed differences in gene dependency, we performed permutation testing by randomly shuffling (8,000 times for each cancer type; 4,000 times for each mutation) the OXPPOS state labels (High and Low) across cell lines participating in each comparison and computing permutation  $P$  values. We then used  $P \leq 0.01$  as the significance cutoff to identify mutations and tissue types associated with enhanced OXPPOS state-specific gene dependencies relative to pan-cancer analysis.

## **Bioinformatics analysis on patient-derived glioma tumors**

Clinical history, mutation profiles, and gene expression correlation were accessed using the cBioPortal for Cancer Genomics (<http://cbioportal.org/>)<sup>53</sup>. Diffuse glioma patient samples from the GLASS Consortium were used for analysis<sup>39</sup>. Diffuse glioma patients were classified based on their PTEN mutation status, resulting in 64 patients with PTEN mutations (PTEN<sup>Mut</sup>) and 158 patients with wildtype PTEN (PTEN<sup>WT</sup>). Of these patients, 57 PTEN<sup>Mut</sup> and 150 PTEN<sup>WT</sup> had survival data. Overall survival of PTEN<sup>Mut</sup> versus PTEN<sup>WT</sup> patients were compared using two-sided  $P$  value computed by log-rank (Mantel–Cox) test. To infer how PTEN expression might be associated with glioma tumor state, we

performed transcriptome-wide co-expression analysis across 79 tumor samples for which RNA-sequencing data were available. We used Spearman's correlation analysis to rank transcripts based on the association of their abundance with PTEN expression. *P* values were then corrected using Benjamini-Hochberg FDR correction. Genes that were negatively or positively correlated with PTEN expression and had  $FDR \leq 0.05$  were selected for gene set enrichment analysis using Enrichr.

### **Single-cell RNA sequencing analysis of glioma tumors**

To test the association of PTEN loss with mitochondrial electron transport chain components at a single-cell level, we analyzed a published single-cell RNA-sequencing dataset of genetically profiled patient-derived glioblastoma tumors<sup>40</sup>. Malignant cells were classified based on the PTEN mutation status, resulting in 10,268 PTEN-mutant cells found in 6 patients and 23,229 PTEN-wildtype cells found in 20 patients. For gene expression analysis, we used the log-normalized gene expression data, as reported by Ruiz-Moreno *et al*<sup>40</sup>, for computing mean gene expression scores. Mean gene expression scores were calculated for every single cell using the follow gene sets: Respiratory Chain Complex I (GO:0045271), Respiratory Chain Complex II (GO:0045273), Respiratory Chain Complex III (GO:0005750), Respiratory Chain Complex IV (GO:0045277), and ATP synthase (GO:0045259). Significance of gene set expression between PTEN-mutant and PTEN-wildtype cells was determined using a one-sided, permutation test (5,000 permutations per test), hypothesizing that PTEN-mutant cells are higher in gene expression compared to PTEN-wildtype. The permutation test MATLAB function was accessed via MathWorks File Exchange (<https://github.com/lrkrol/permutationTest>; retrieved 13 September 2023).

### **Drug sensitivity analysis**

To test the impact of damaging mutations in PTEN on OXPHOS state-specific dependencies, we used

the Cancer Therapeutics Response Portal (CTRP) data to analyze the sensitivity of 799 genetically characterized cancer cell lines to 545 small-molecule probes and drugs<sup>32</sup>. We used transcriptomics data to define groups of OXPPOS<sup>Low</sup> and OXPPOS<sup>High</sup> cell lines based on whether their OXPPOS state scores were ranked within the top or bottom 33 percentiles. We then compared the median sensitivity of OXPPOS<sup>Low</sup> and OXPPOS<sup>High</sup> cell lines to each tested small molecule based on the area of the dose-response curve (AUC) measurements. Within the OXPPOS<sup>High</sup> group, we also compared the median sensitivity of PTEN-wildtype (PTEN<sup>WT</sup>) and PTEN-mutated (PTEN<sup>Mut</sup>) subgroups. Significance of comparison was determined using one-sided Wilcoxon rank sum test by MATLAB function *ranksum*.

### **Hierarchical clustering**

Unsupervised hierarchical clustering of pathway activity scores and *P* values from pre-rank GSEA were carried out in R using the *heatmap* package (1.0.12). Clustering was performed using the *heatmap* function using default settings with Euclidean distance metric.

### **Software**

Statistical analyses were performed using MATLAB (2022b), R (4.1.1), and RStudio (2022.07.2).

### **Data availability**

RNA sequencing data for cell lines in the Cancer Cell Line Encyclopedia (CCLE) were downloaded from the Cancer Dependency Map (DepMap) portal (<https://depmap.org/portal/>; filename: OmicsExpressionProteinCodingGenesTPMLogp1.csv, 23Q2 release). Growth media metadata was downloaded from DepMap portal (filenames: Media.csv, Model.csv, 23Q2 release). Gene knockout effect data (i.e., gene dependency scores) were downloaded from DepMap portal (filename:

CRISPRGeneDependency.csv, 23Q2 release). CCLE mutation data were downloaded from DepMap portal (filename: OmicsSomaticMutations.csv, 23Q2 release). Drug sensitivity (AUC) data, originally released by the Cancer Therapeutics Response Portal (CTRP), were downloaded from the NCI CTD<sup>2</sup> Data Portal (<https://ocg.cancer.gov/programs/ctd2/data-portal>; filename: CTRPv2.0\_2015\_ctd2\_ExpandedDataset.zip). The single-cell RNA sequencing data from glioma tumors were accessed from CELLxGENE (<https://cellxgene.cziscience.com/>; Dataset: Harmonized single-cell landscape, intercellular crosstalk and tumor architecture of glioblastoma; file: Core GBMap rds, accessed 27 August 2023). Single cells were selected for further analysis if their cell type was “malignant cell” and their PTEN mutation status was “mutated” or “no mutated.”

## **Code availability**

The original codes for data analysis performed in this paper are publicly available at <https://github.com/fallahi-sichani-lab/metabolicStateVulnerabilities>.

## **Acknowledgments**

We thank D. Kashatus, members of the Fallahi-Sichani laboratory and the Systems Analysis of Stress-adapted Cancer Organelles (SASCO) Center at the University of Virginia for helpful discussion and suggestions. This work was supported by NIH grants R35-GM133404 and R01-CA249229 (to M.F.-S.), and the University of Michigan Rackham Merit Fellowship (to C.A.).

## **Author Contributions**

C.A. and M.F.-S. conceived and designed the study, performed computational model analysis, and wrote the manuscript. M.F.-S. supervised the work.

## State of Competing Interests

The authors declare that they have no competing interests.

## Figure Legends

### **Figure 1. UMAP analysis of metabolic gene expression reveals clusters of cancer cell lines**

**associated with cancer type and developmental lineage.** (A) Total 1,341 CCLE cell lines, representing 41 cancer types, were included in the analysis. Number of cell lines for each cancer type are shown. (B) UMAP visualization of cell lines based on the expression levels of 1,620 metabolic genes. Cell lines are colored based on their cancer type (as shown in A). (C) Examples of metabolic similarities across tumor lineages (top) or heterogeneities within cancer types (bottom) are shown. Individual cell lines from indicated cancer types are highlighted on UMAP plots.

### **Figure 2. Metabolic pathway analysis of cancer cell lines reveals cancer type-associated variations**

**in the activity of pathways.** (A) Hierarchical clustering of relative activity scores for 73 significantly variable metabolic pathways across 41 cancer types. A metabolic pathway activity score  $< 1$  for a cancer type represents reduced pathway activity in that cancer type in comparison with the average pathway activity across all cancer types; scores  $> 1$  represent increased activity; and a score of 1 represents activity levels equivalent to the average over all cancer types. (B) Ranking of metabolic pathways based on the extent to which their heterogeneity is associated with cancer type, evaluated by computing the absolute sum of PCA loadings for each pathway over the first eight principal components. The top 5 and bottom 5 variable pathways are shown.

**Figure 3. OXPPOS state exhibits substantial cell line-to-cell line heterogeneity independent of cancer type.** (A) Metabolic pathways enriched in genes with highest contribution (determined by PCA) to the metabolic heterogeneities among individual cell lines from different cancer types. Data are clustered based on  $-\log_{10}(\text{FDR})$  values derived from gene set enrichment analysis (GSEA). Pairs of pathway/cancer type with significant cell line-to-cell line heterogeneity ( $\text{FDR} \leq 0.05$ ) are highlighted with an asterisk (\*). (B) Metabolic pathways ranked according to the % of cancer types showing significant cell line-to-cell line heterogeneity. (C) Distinct patterns of cell line-to-cell line variability in two representative metabolic pathways, ascorbate and aldarate metabolism (left) and oxidative phosphorylation (right), across indicated cancer types. Mean pathway transcript per million (TPM) levels, their median and interquartile ranges (IQR) across cell lines are highlighted.

**Figure 4. Metabolic pathway analysis of cancer cell lines reveals variations in the activity of pathways associated with growth media.** (A) Hierarchical clustering of relative activity scores for 73 significantly variable metabolic pathways across 21 chemically distinct growth media. A metabolic pathway activity score  $< 1$  for a growth medium represents reduced pathway activity in that growth medium in comparison with the average pathway activity across all growth media; scores  $> 1$  represent increased activity; and a score of 1 represents activity levels equivalent to the average over all growth media. (B) Ranking of metabolic pathways based on the extent to which their heterogeneity is associated with growth media, evaluated by computing the absolute sum of PCA loadings for each pathway over the first four principal components.

**Figure 5. Multivariate modeling uncovers pan-cancer gene vulnerabilities associated with OXPPOS state.** (A) The top enriched biochemical pathways (from Reactome Pathway Database)

associated with gene vulnerability features selected by elastic net regularization ( $FDR \leq 0.05$ ). Genes with positive and negative elastic net coefficients were used to infer vulnerabilities in OXPPOS<sup>High</sup> and OXPPOS<sup>Low</sup> cell lines, respectively. **(B)** Performance of the partial least squares (PLSR) model evaluated by variance in OXPPOS state scores explained ( $R^2$ ) or predicted based on leave-one-out cross-validation ( $Q^2$ ) with increasing number of PLS components. **(C)** Comparison between OXPPOS state scores and predicted scores by PLSR for the training set of 296 cell lines (left) and independent test set of 32 cell lines (right). Two-sided Pearson's correlation analysis was performed between OXPPOS state scores and PLSR predicted scores. **(D)** PLSR scores colored according to their OXPPOS state score. **(E)** The list of pan-cancer gene vulnerabilities strongly associated with the OXPPOS<sup>High</sup> or OXPPOS<sup>Low</sup> state. For each gene, the median difference between dependency ( $\Delta$  gene dependency) for OXPPOS<sup>High</sup> and OXPPOS<sup>Low</sup> subgroups of cell lines are shown.

**Figure 6. Statistical analysis reveals synthetically lethal associations between OXPPOS state, driver mutations and tissue context.** **(A)** Statistical enrichment of OXPPOS<sup>High</sup>-associated mitochondrial gene vulnerabilities in cell lines associated with specific tissue types or driver mutations. Enrichment is considered significant if the median gene dependency difference ( $\Delta$  gene dependency) between OXPPOS<sup>High</sup> and OXPPOS<sup>Low</sup> subgroups of cell lines associated with a cancer type or driver mutation is significantly larger than the median gene dependency difference between OXPPOS<sup>High</sup> and OXPPOS<sup>Low</sup> groups regardless of cancer type and mutation (i.e., pan-cancer median difference level highlighted by the black circle and dotted line). Statistical significance of median differences was determined by empirical  $P$  values computed based on permutation testing. **(B)** The impact of PTEN mutation on mitochondrial gene dependencies in OXPPOS<sup>High</sup> and OXPPOS<sup>Low</sup> cell lines. Statistical significance of median differences was determined by empirical  $P$  values computed based on

permutation testing. **(C)** Statistical enrichment of OXPHOS<sup>High</sup>-associated EP300 dependency in cell lines associated with specific tissue types or driver mutations. Statistical significance of median differences was determined by empirical *P* values computed based on permutation testing. **(D)** Statistical enrichment of OXPHOS<sup>Low</sup>-associated gene vulnerabilities in cell lines associated with specific tissue types or driver mutations. Statistical significance of median differences was determined by empirical *P* values computed based on permutation testing.

**Figure 7. Loss of PTEN predicts increased dependency on mitochondrial respiratory chain in OXPHOS<sup>High</sup> tumor cells.** **(A)** Analysis of the Cancer Therapeutics Response Portal (CTRP) data, including sensitivity measurements (evaluated based on area under the dose response curve; AUC) for 545 small-molecule probes and drugs in 799 cell lines. For each compound, the difference in median sensitivity ( $\Delta$  drug AUC) between OXPHOS<sup>Low</sup> and OXPHOS<sup>High</sup> subgroups of cell lines is shown against the difference in median sensitivity between OXPHOS<sup>High</sup>/PTEN<sup>WT</sup> and OXPHOS<sup>High</sup>/PTEN<sup>Mut</sup> subgroups. Statistical significance was determined using one-sided Wilcoxon rank sum test. **(B)** Overall survival analysis of glioma patients with PTEN-mutated (PTEN<sup>Mut</sup>) or PTEN-wildtype (PTEN<sup>WT</sup>) tumors. Statistical significance was determined by two-sided log-rank (Mantel-Cox) test. **(C)** The top Gene Ontology (GO) biological processes ( $FDR \leq 0.05$ ) associated with genes whose expression negatively correlated with PTEN mRNA levels across 79 glioma tumors. **(D)** Single-cell analysis of PTEN<sup>Mut</sup> versus PTEN<sup>WT</sup> glioma tumors. Mean log-normalized levels of transcripts representing individual components of the electron transport chain, including Complex I-IV and ATP synthase, between PTEN<sup>Mut</sup> ( $n = 10,268$ ) and PTEN<sup>WT</sup> ( $n = 23,229$ ) malignant cells. Statistical significance was determined by one-sided, permutation test.

## Supplementary Figure Legends

### **Figure S1. UMAP analysis of metabolic gene expression reveals clusters of cancer cell lines**

#### **associated with cancer type and developmental lineage. Related to Figure 1. (A) UMAP**

visualization of cell lines based on the expression levels of 1,620 metabolic genes. Cell lines are colored based on their cancer type. **(B)** Non-Small Cell Lung Cancer (NSCLC) cell lines and their subtypes, including Giant Cell Carcinoma of the Lung, Large Cell Lung Carcinoma, Lung Adenocarcinoma, Lung Adenosquamous Carcinoma, Lung Squamous Cell Carcinoma, Mucoepidermoid Carcinoma of the Lung, Non-Small Cell Lung Cancer, and Poorly Differentiated Non-Small Cell Lung Cancer, are highlighted on UMAP plot.

### **Figure S2. Variability of the overall metabolic activity across cell lines of different cancer types.**

#### **Related to Figure 2. (A) Calculated metabolic activity scores (original, non-permuted scores) of 73**

pathways across 41 cancer types. A metabolic pathway activity score  $< 1$  for a cancer type represents reduced pathway activity in that cancer type in comparison with the average pathway activity across all cancer types; scores  $> 1$  represent increased activity; and a score of 1 represents activity levels equivalent to the average over all cancer types. **(B)** Principal component analysis (PCA) of metabolic pathway activity scores across 41 cancer types. Percentage of variance captured by the first eight principal components (PC) are shown. **(C)** Ranking of metabolic pathways based on the extent to which their heterogeneity is associated with cancer type, evaluated by computing the absolute sum of PCA loadings for each pathway over the first eight principal components.

### **Figure S3. Distinct patterns of cell line-to-cell line variability in two representative metabolic**

**pathways. Related to Figure 3.** The data are shown for oxidative phosphorylation (top) and ascorbate

and aldarate metabolism (bottom) across indicated cancer types. Mean pathway transcript per million (TPM) levels, their median and interquartile ranges (IQR) across cell lines are highlighted.

**Figure S4. Principal component analysis (PCA) of metabolic pathway activity scores across 21 distinct growth media. Related to Figure 4.** Percentage of variance captured by the first four principal components (PC) are shown.

**Figure S5. Elastic net regularization selects a subset of gene features based on their association with the OXPHOS state score across cell lines. Related to Figure 5.** (A) Distribution of oxidative phosphorylation (OXPHOS) states scores across 495 cell lines. OXPHOS<sup>High</sup> and OXPHOS<sup>Low</sup> groups of cell lines (each containing 164 cell lines) were determined based on the top and bottom 33 percentiles. (B) Distribution of interquartile ranges (IQR) of gene dependency scores for 17,202 genes. IQR for each gene was calculated across 328 cell lines. IQR threshold (dotted red line) and remaining genes after IQR filtering (right of the dotted red line) are shown. (C) Distribution of OXPHOS states scores across randomly selected training set (296 cell lines) and test set (32 cell lines). (D) Optimization of elastic net model parameter  $\alpha$ . Boxplots of mean squared error (MSE) across 150 elastic net iterations (for each  $\alpha$ ) with varying  $\alpha$  values of 0.1 to 0.9. (E) Fraction of occurrence for a given gene appearing across 150 random elastic net iterations. Genes that occurred in at least 50% of the iterations were used in the next step (i.e., PLSR modeling). (F) The top enriched GO cellular components associated with gene vulnerability features selected by elastic net regularization ( $P \leq 0.05$ ). Genes with positive and negative elastic net coefficients were used to infer vulnerabilities in OXPHOS<sup>High</sup> and OXPHOS<sup>Low</sup> cell lines, respectively. (G) PLSR-derived VIP scores  $\geq 1$  or  $\leq -1$ . The sign of the VIP scores shows whether the identified gene is a vulnerability in OXPHOS<sup>High</sup> cell lines (red) or OXPHOS<sup>Low</sup> cell lines (blue).

**Figure S6. Statistical analysis reveals synthetically lethal associations between OXPPOS state, driver mutations and tissue context. Related to Figure 6. (A)** The number of cell lines bearing each of the top 25 most frequent driver mutations across eleven OXPPOS-variable cancer types. Total mutation frequency for each of the 25 mutations is shown on the bottom. Total number of cell lines for each OXPPOS-variable cancer type is shown on the right. **(B)** The top 25 most frequent driver mutations and their associated frequencies across OXPPOS<sup>High</sup> and OXPPOS<sup>Low</sup> cell lines. Number of cell lines that have a given mutation is shown next to each bar. **(C, D)** Statistical enrichment of OXPPOS<sup>High</sup>-associated **(C)** and OXPPOS<sup>Low</sup>-associated **(D)** gene vulnerabilities in cell lines associated with specific tissue types or driver mutations. Enrichment is considered significant if the median gene dependency difference ( $\Delta$  gene dependency) between OXPPOS<sup>High</sup> and OXPPOS<sup>Low</sup> subgroups of cell lines associated with a cancer type or driver mutation is significantly larger than the median gene dependency difference between OXPPOS<sup>High</sup> and OXPPOS<sup>Low</sup> groups regardless of cancer type and mutation (i.e., pan-cancer median difference level highlighted by the black circle and dotted line). Statistical significance of median differences was determined by empirical *P* values computed based on permutation testing.

**Figure S7. Loss of PTEN predicts increased dependency on mitochondrial respiratory chain in OXPPOS<sup>High</sup> tumor cells. Related to Figure 7. (A)** Spearman's correlation analysis to rank transcripts based on the association of their abundance with PTEN expression in 79 patient-derived glioma tumors. Transcripts negatively correlated (blue) or positively correlated (red) with PTEN mRNA levels were highlighted as significant if  $FDR \leq 0.05$ . **(B)** The top Gene Ontology (GO) cellular components ( $FDR \leq 0.05$ ) associated with genes whose expression negatively correlated with PTEN mRNA levels across 79

glioma tumors. **(C, D)** The top GO biological processes **(C)** or cellular components **(D)** associated with genes whose expression positively correlated with PTEN mRNA levels across 79 glioma tumors ( $FDR \leq 0.05$ ).

## References

1. Finley, L.W.S. (2023). What is cancer metabolism? *Cell* *186*, 1670–1688. [10.1016/j.cell.2023.01.038](https://doi.org/10.1016/j.cell.2023.01.038).
2. Stine, Z.E., Schug, Z.T., Salvino, J.M., and Dang, C.V. (2022). Targeting cancer metabolism in the era of precision oncology. *Nat Rev Drug Discov* *21*, 141–162. [10.1038/s41573-021-00339-6](https://doi.org/10.1038/s41573-021-00339-6).
3. Bi, J., Wu, S., Zhang, W., and Mischel, P.S. (2018). Targeting cancer's metabolic co-dependencies: A landscape shaped by genotype and tissue context. *Biochim Biophys Acta Rev Cancer* *1870*, 76–87. [10.1016/j.bbcan.2018.05.002](https://doi.org/10.1016/j.bbcan.2018.05.002).
4. Fendt, S.-M., Frezza, C., and Erez, A. (2020). Targeting Metabolic Plasticity and Flexibility Dynamics for Cancer Therapy. *Cancer Discovery* *10*, 1797–1807. [10.1158/2159-8290.CD-20-0844](https://doi.org/10.1158/2159-8290.CD-20-0844).
5. Kondo, H., Ratcliffe, C.D.H., Hooper, S., Ellis, J., MacRae, J.I., Hennequart, M., Dunsby, C.W., Anderson, K.I., and Sahai, E. (2021). Single-cell resolved imaging reveals intra-tumor heterogeneity in glycolysis, transitions between metabolic states, and their regulatory mechanisms. *Cell Reports* *34*, 108750. [10.1016/j.celrep.2021.108750](https://doi.org/10.1016/j.celrep.2021.108750).
6. Rohle, D., Popovici-Muller, J., Palaskas, N., Turcan, S., Grommes, C., Campos, C., Tsoi, J., Clark, O., Oldrini, B., Komisopoulou, E., et al. (2013). An inhibitor of mutant IDH1 delays growth and promotes differentiation of glioma cells. *Science* *340*, 626–630. [10.1126/science.1236062](https://doi.org/10.1126/science.1236062).
7. Yen, K., Travins, J., Wang, F., David, M.D., Artin, E., Straley, K., Padyana, A., Gross, S., DeLaBarre, B., Tobin, E., et al. (2017). AG-221, a First-in-Class Therapy Targeting Acute Myeloid Leukemia Harboring Oncogenic IDH2 Mutations. *Cancer Discov* *7*, 478–493. [10.1158/2159-8290.CD-16-1034](https://doi.org/10.1158/2159-8290.CD-16-1034).
8. Kim, J., Hu, Z., Cai, L., Li, K., Choi, E., Faubert, B., Bezwada, D., Rodriguez-Canales, J., Villalobos, P., Lin, Y.-F., et al. (2017). CPS1 maintains pyrimidine pools and DNA synthesis in KRAS/LKB1-mutant lung cancer cells. *Nature* *546*, 168–172. [10.1038/nature22359](https://doi.org/10.1038/nature22359).
9. Nwosu, Z.C., Ward, M.H., Sajjakulnukit, P., Poudel, P., Ragulan, C., Kasperek, S., Radyk, M., Sutton, D., Menjivar, R.E., Andren, A., et al. (2023). Uridine-derived ribose fuels glucose-restricted pancreatic cancer. *Nature* *618*, 151–158. [10.1038/s41586-023-06073-w](https://doi.org/10.1038/s41586-023-06073-w).

10. Gwynne, W.D., Suk, Y., Custers, S., Mikolajewicz, N., Chan, J.K., Zador, Z., Chafe, S.C., Zhai, K., Escudero, L., Zhang, C., et al. (2022). Cancer-selective metabolic vulnerabilities in MYC-amplified medulloblastoma. *Cancer Cell* *40*, 1488-1502.e7. 10.1016/j.ccell.2022.10.009.
11. Li, H., Ning, S., Ghandi, M., Kryukov, G.V., Gopal, S., Deik, A., Souza, A., Pierce, K., Keskula, P., Hernandez, D., et al. (2019). The landscape of cancer cell line metabolism. *Nat Med* *25*, 850–860. 10.1038/s41591-019-0404-8.
12. Ghandi, M., Huang, F.W., Jané-Valbuena, J., Kryukov, G.V., Lo, C.C., McDonald, E.R., Barretina, J., Gelfand, E.T., Bielski, C.M., Li, H., et al. (2019). Next-generation characterization of the Cancer Cell Line Encyclopedia. *Nature* *569*, 503–508. 10.1038/s41586-019-1186-3.
13. Joly, J.H., Chew, B.T.L., and Graham, N.A. (2021). The landscape of metabolic pathway dependencies in cancer cell lines. *PLoS Comput Biol* *17*, e1008942. 10.1371/journal.pcbi.1008942.
14. Lagziel, S., Lee, W.D., and Shlomi, T. (2019). Inferring cancer dependencies on metabolic genes from large-scale genetic screens. *BMC Biol* *17*, 37. 10.1186/s12915-019-0654-4.
15. Cherkaoui, S., Durot, S., Bradley, J., Critchlow, S., Dubuis, S., Masiero, M.M., Wegmann, R., Snijder, B., Othman, A., Bendtsen, C., et al. (2022). A functional analysis of 180 cancer cell lines reveals conserved intrinsic metabolic programs. *Molecular Systems Biology* *18*, e11033. 10.15252/msb.202211033.
16. Shorthouse, D., Bradley, J., Critchlow, S.E., Bendtsen, C., and Hall, B.A. (2022). Heterogeneity of the cancer cell line metabolic landscape. *Molecular Systems Biology* *18*, e11006. 10.15252/msb.202211006.
17. Pemovska, T., Bigenzahn, J.W., Srndic, I., Lercher, A., Bergthaler, A., César-Razquin, A., Kartnig, F., Kornauth, C., Valent, P., Staber, P.B., et al. (2021). Metabolic drug survey highlights cancer cell dependencies and vulnerabilities. *Nat Commun* *12*, 7190. 10.1038/s41467-021-27329-x.
18. Yang, J., Griffin, A., Qiang, Z., and Ren, J. (2022). Organelle-targeted therapies: a comprehensive review on system design for enabling precision oncology. *Signal Transduct Target Ther* *7*, 379. 10.1038/s41392-022-01243-0.
19. Benedetti, E., Liu, E.M., Tang, C., Kuo, F., Buyukozkan, M., Park, T., Park, J., Correa, F., Hakimi, A.A., Intlekofer, A.M., et al. (2023). A multimodal atlas of tumour metabolism reveals the architecture of gene-metabolite covariation. *Nat Metab* *5*, 1029–1044. 10.1038/s42255-023-00817-8.
20. Campit, S.E., Bhowmick, R., Lu, T., Saoji, A.V., Jin, R., Robida, A.M., and Chandrasekaran, S. (2023). Data-Driven Screening to Infer Metabolic Modulators of the Cancer Epigenome (Systems Biology) 10.1101/2023.02.27.530260.
21. Sessions, D.T., Kim, K.-B., Kashatus, J.A., Churchill, N., Park, K.-S., Mayo, M.W., Sesaki, H., and Kashatus, D.F. (2022). Opa1 and Drp1 reciprocally regulate cristae morphology, ETC function, and NAD<sup>+</sup> regeneration in KRas-mutant lung adenocarcinoma. *Cell Rep* *41*, 111818. 10.1016/j.celrep.2022.111818.

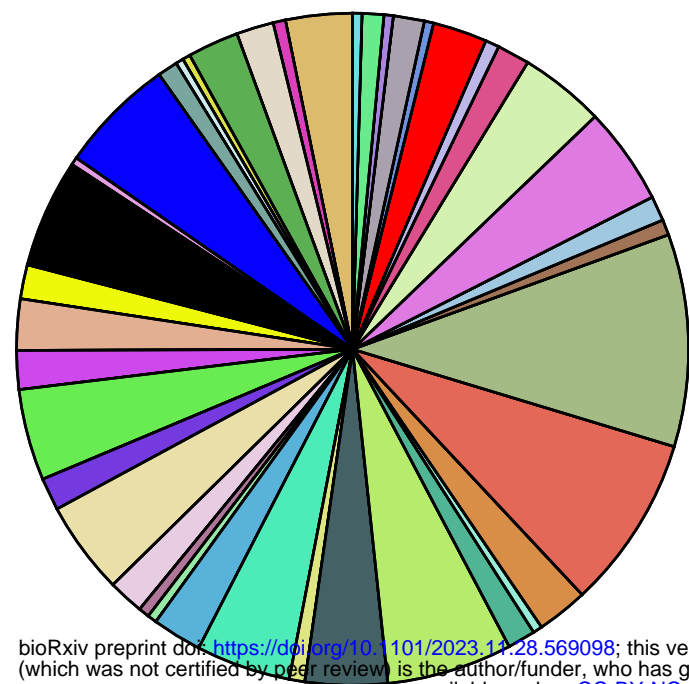
22. Barretina, J., Caponigro, G., Stransky, N., Venkatesan, K., Margolin, A.A., Kim, S., Wilson, C.J., Lehár, J., Kryukov, G.V., Sonkin, D., et al. (2012). The Cancer Cell Line Encyclopedia enables predictive modelling of anticancer drug sensitivity. *Nature* 483, 603–607. 10.1038/nature11003.
23. Becht, E., McInnes, L., Healy, J., Dutertre, C.-A., Kwok, I.W.H., Ng, L.G., Ginhoux, F., and Newell, E.W. (2019). Dimensionality reduction for visualizing single-cell data using UMAP. *Nat Biotechnol* 37, 38–44. 10.1038/nbt.4314.
24. Kanehisa, M., Sato, Y., Kawashima, M., Furumichi, M., and Tanabe, M. (2016). KEGG as a reference resource for gene and protein annotation. *Nucleic Acids Research* 44, D457–D462. 10.1093/nar/gkv1070.
25. Xiao, Z., Dai, Z., and Locasale, J.W. (2019). Metabolic landscape of the tumor microenvironment at single cell resolution. *Nat Commun* 10, 3763. 10.1038/s41467-019-11738-0.
26. Ackermann, T., and Tardito, S. (2019). Cell Culture Medium Formulation and Its Implications in Cancer Metabolism. *Trends Cancer* 5, 329–332. 10.1016/j.trecan.2019.05.004.
27. Dempster, J.M., Boyle, I., Vazquez, F., Root, D.E., Boehm, J.S., Hahn, W.C., Tsherniak, A., and McFarland, J.M. (2021). Chronos: a cell population dynamics model of CRISPR experiments that improves inference of gene fitness effects. *Genome Biology* 22, 343. 10.1186/s13059-021-02540-7.
28. Gunn, B.M., Yu, W.-H., Karim, M.M., Brannan, J.M., Herbert, A.S., Wec, A.Z., Halfmann, P.J., Fusco, M.L., Schendel, S.L., Gangavarapu, K., et al. (2018). A Role for Fc Function in Therapeutic Monoclonal Antibody-Mediated Protection against Ebola Virus. *Cell Host & Microbe* 24, 221–233.e5. 10.1016/j.chom.2018.07.009.
29. Selva, K.J., van de Sandt, C.E., Lemke, M.M., Lee, C.Y., Shoffner, S.K., Chua, B.Y., Davis, S.K., Nguyen, T.H.O., Rowntree, L.C., Hensen, L., et al. (2021). Systems serology detects functionally distinct coronavirus antibody features in children and elderly. *Nat Commun* 12, 2037. 10.1038/s41467-021-22236-7.
30. Zhang, L., Cao, J., Dong, L., and Lin, H. (2020). TiPARP forms nuclear condensates to degrade HIF-1 $\alpha$  and suppress tumorigenesis. *Proc Natl Acad Sci U S A* 117, 13447–13456. 10.1073/pnas.1921815117.
31. Mendiratta, G., Ke, E., Aziz, M., Liarakos, D., Tong, M., and Stites, E.C. (2021). Cancer gene mutation frequencies for the U.S. population. *Nat Commun* 12, 5961. 10.1038/s41467-021-26213-y.
32. Rees, M.G., Seashore-Ludlow, B., Cheah, J.H., Adams, D.J., Price, E.V., Gill, S., Javaid, S., Coletti, M.E., Jones, V.L., Bodycombe, N.E., et al. (2016). Correlating chemical sensitivity and basal gene expression reveals mechanism of action. *Nat Chem Biol* 12, 109–116. 10.1038/nchembio.1986.
33. Linnett, P.E., and Beechey, R.B. (1979). Inhibitors of the ATP synthetase systems. In *Methods in Enzymology* (Elsevier), pp. 472–518. 10.1016/0076-6879(79)55061-7.

34. Ulanovskaya, O.A., Janjic, J., Suzuki, M., Sabharwal, S.S., Schumacker, P.T., Kron, S.J., and Kozmin, S.A. (2008). Synthesis enables identification of the cellular target of leucascandrolide A and neopeltolide. *Nat Chem Biol* 4, 418–424. 10.1038/nchembio.94.
35. Jonsson, P., Lin, A.L., Young, R.J., DiStefano, N.M., Hyman, D.M., Li, B.T., Berger, M.F., Zehir, A., Ladanyi, M., Solit, D.B., et al. (2019). Genomic Correlates of Disease Progression and Treatment Response in Prospectively Characterized Gliomas. *Clin Cancer Res* 25, 5537–5547. 10.1158/1078-0432.CCR-19-0032.
36. Shi, Y., Lim, S.K., Liang, Q., Iyer, S.V., Wang, H.-Y., Wang, Z., Xie, X., Sun, D., Chen, Y.-J., Tabar, V., et al. (2019). Gboxin is an oxidative phosphorylation inhibitor that targets glioblastoma. *Nature* 567, 341–346. 10.1038/s41586-019-0993-x.
37. Molina, J.R., Sun, Y., Protopopova, M., Gera, S., Bandi, M., Bristow, C., McAfoos, T., Morlacchi, P., Ackroyd, J., Agip, A.-N.A., et al. (2018). An inhibitor of oxidative phosphorylation exploits cancer vulnerability. *Nat Med* 24, 1036–1046. 10.1038/s41591-018-0052-4.
38. Sesen, J., Dahan, P., Scotland, S.J., Saland, E., Dang, V.-T., Lemarié, A., Tyler, B.M., Brem, H., Toulas, C., Cohen-Jonathan Moyal, E., et al. (2015). Metformin inhibits growth of human glioblastoma cells and enhances therapeutic response. *PLoS One* 10, e0123721. 10.1371/journal.pone.0123721.
39. Barthel, F.P., Johnson, K.C., Varn, F.S., Moskalik, A.D., Tanner, G., Kocakavuk, E., Anderson, K.J., Abiola, O., Aldape, K., Alfaro, K.D., et al. (2019). Longitudinal molecular trajectories of diffuse glioma in adults. *Nature* 576, 112–120. 10.1038/s41586-019-1775-1.
40. Ruiz-Moreno, C., Salas, S.M., Samuelsson, E., Brandner, S., Kranendonk, M.E.G., Nilsson, M., and Stunnenberg, H.G. (2022). Harmonized single-cell landscape, intercellular crosstalk and tumor architecture of glioblastoma (*Cancer Biology*) 10.1101/2022.08.27.505439.
41. Mahendralingam, M.J., Kim, H., McCloskey, C.W., Aliar, K., Casey, A.E., Tharmapalan, P., Pellacani, D., Ignatchenko, V., Garcia-Valero, M., Palomero, L., et al. (2021). Mammary epithelial cells have lineage-rooted metabolic identities. *Nat Metab* 3, 665–681. 10.1038/s42255-021-00388-6.
42. Han, M., Bushong, E.A., Segawa, M., Tiard, A., Wong, A., Brady, M.R., Momcilovic, M., Wolf, D.M., Zhang, R., Petcherski, A., et al. (2023). Spatial mapping of mitochondrial networks and bioenergetics in lung cancer. *Nature* 615, 712–719. 10.1038/s41586-023-05793-3.
43. Cogliati, S., Frezza, C., Soriano, M.E., Varanita, T., Quintana-Cabrera, R., Corrado, M., Cipolat, S., Costa, V., Casarin, A., Gomes, L.C., et al. (2013). Mitochondrial cristae shape determines respiratory chain supercomplexes assembly and respiratory efficiency. *Cell* 155, 160–171. 10.1016/j.cell.2013.08.032.
44. Anderson, G.R., Wardell, S.E., Cakir, M., Yip, C., Ahn, Y.-R., Ali, M., Yllanes, A.P., Chao, C.A., McDonnell, D.P., and Wood, K.C. (2018). Dysregulation of mitochondrial dynamics proteins are a targetable feature of human tumors. *Nat Commun* 9, 1677. 10.1038/s41467-018-04033-x.

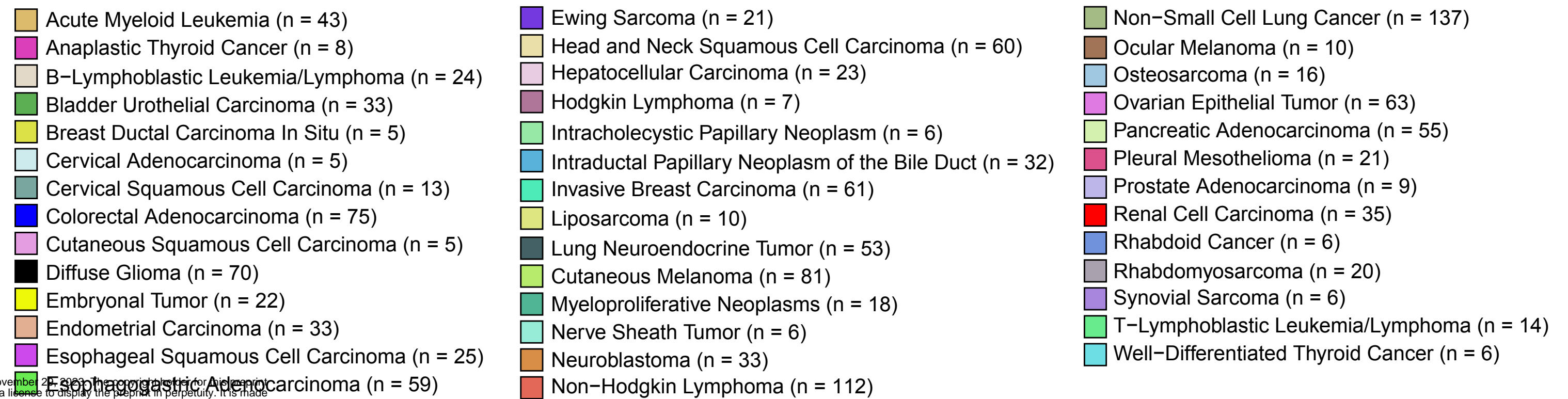
45. Naguib, A., Mathew, G., Reczek, C.R., Watrud, K., Ambrico, A., Herzka, T., Salas, I.C., Lee, M.F., El-Amine, N., Zheng, W., et al. (2018). Mitochondrial Complex I Inhibitors Expose a Vulnerability for Selective Killing of Pten-Null Cells. *Cell Rep* 23, 58–67. [10.1016/j.celrep.2018.03.032](https://doi.org/10.1016/j.celrep.2018.03.032).
46. Yap, T.A., Daver, N., Mahendra, M., Zhang, J., Kamiya-Matsuoka, C., Meric-Bernstam, F., Kantarjian, H.M., Ravandi, F., Collins, M.E., Francesco, M.E.D., et al. (2023). Complex I inhibitor of oxidative phosphorylation in advanced solid tumors and acute myeloid leukemia: phase I trials. *Nat Med* 29, 115–126. [10.1038/s41591-022-02103-8](https://doi.org/10.1038/s41591-022-02103-8).
47. Machado, N.D., Heather, L.C., Harris, A.L., and Higgins, G.S. (2023). Targeting mitochondrial oxidative phosphorylation: lessons, advantages, and opportunities. *Br J Cancer* 129, 897–899. [10.1038/s41416-023-02394-9](https://doi.org/10.1038/s41416-023-02394-9).
48. Garofano, L., Migliozzi, S., Oh, Y.T., D’Angelo, F., Najac, R.D., Ko, A., Frangaj, B., Caruso, F.P., Yu, K., Yuan, J., et al. (2021). Pathway-based classification of glioblastoma uncovers a mitochondrial subtype with therapeutic vulnerabilities. *Nat Cancer* 2, 141–156. [10.1038/s43018-020-00159-4](https://doi.org/10.1038/s43018-020-00159-4).
49. Sighel, D., Notarangelo, M., Aibara, S., Re, A., Ricci, G., Guida, M., Soldano, A., Adami, V., Ambrosini, C., Broso, F., et al. (2021). Inhibition of mitochondrial translation suppresses glioblastoma stem cell growth. *Cell Rep* 35, 109024. [10.1016/j.celrep.2021.109024](https://doi.org/10.1016/j.celrep.2021.109024).
50. Bi, J., Chowdhry, S., Wu, S., Zhang, W., Masui, K., and Mischel, P.S. (2020). Altered cellular metabolism in gliomas - an emerging landscape of actionable co-dependency targets. *Nat Rev Cancer* 20, 57–70. [10.1038/s41568-019-0226-5](https://doi.org/10.1038/s41568-019-0226-5).
51. Kuleshov, M.V., Jones, M.R., Rouillard, A.D., Fernandez, N.F., Duan, Q., Wang, Z., Koplev, S., Jenkins, S.L., Jagodnik, K.M., Lachmann, A., et al. (2016). Enrichr: a comprehensive gene set enrichment analysis web server 2016 update. *Nucleic Acids Res* 44, W90–W97. [10.1093/nar/gkw377](https://doi.org/10.1093/nar/gkw377).
52. Wold, S. (1994). Exponentially weighted moving principal components analysis and projections to latent structures. *Chemometrics and Intelligent Laboratory Systems* 23, 149–161. [10.1016/0169-7439\(93\)E0075-F](https://doi.org/10.1016/0169-7439(93)E0075-F).
53. Cerami, E., Gao, J., Dogrusoz, U., Gross, B.E., Sumer, S.O., Aksoy, B.A., Jacobsen, A., Byrne, C.J., Heuer, M.L., Larsson, E., et al. (2012). The cBio Cancer Genomics Portal: An Open Platform for Exploring Multidimensional Cancer Genomics Data. *Cancer Discovery* 2, 401–404. [10.1158/2159-8290.CD-12-0095](https://doi.org/10.1158/2159-8290.CD-12-0095).

**A**

Total 1341 CCLE cell lines  
41 cancer types



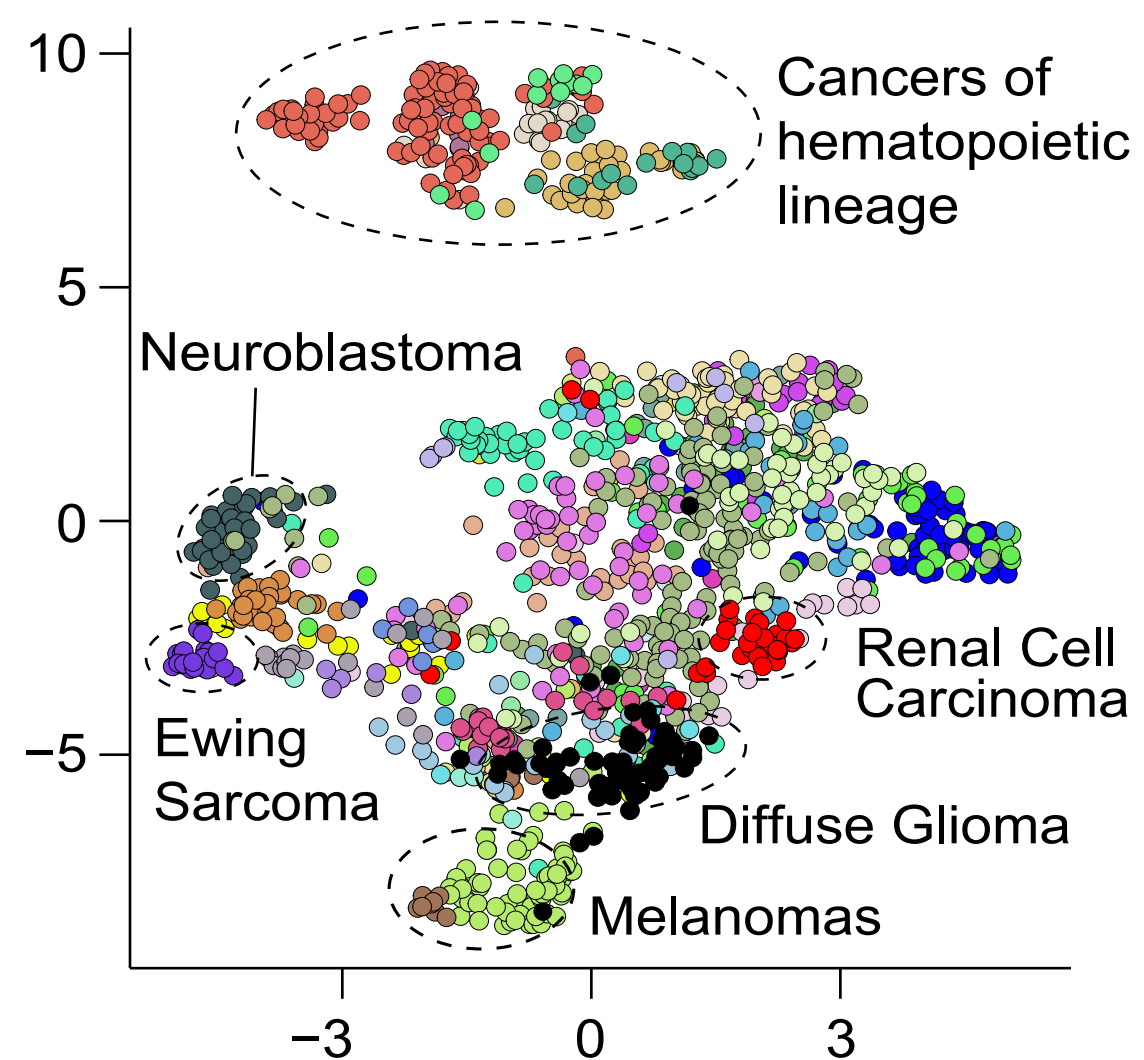
Cancer types



bioRxiv preprint doi: <https://doi.org/10.1101/2023.11.28.569098>; this version posted November 27, 2023. The copyright holder for this preprint (which was not certified by peer review) is the author/funder, who has granted bioRxiv a license to display the preprint in perpetuity. It is made available under aCC-BY-NC-ND 4.0 International license.

**B**

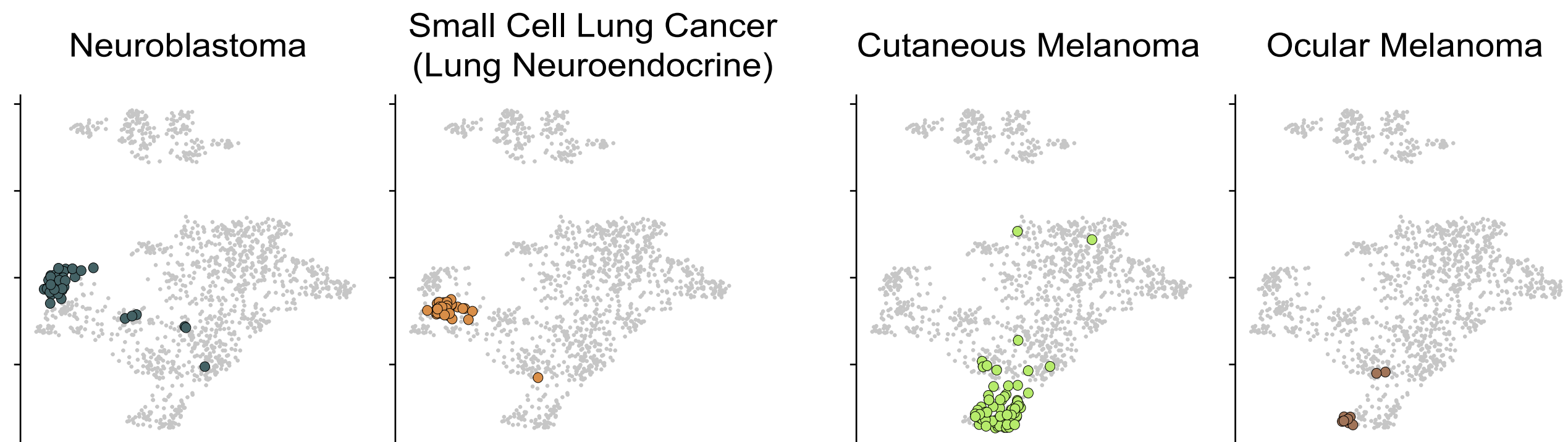
UMAP based on 1620 metabolic genes

**C**

Examples of metabolic similarities across solid tumor lineages

Neuroendocrine lineage

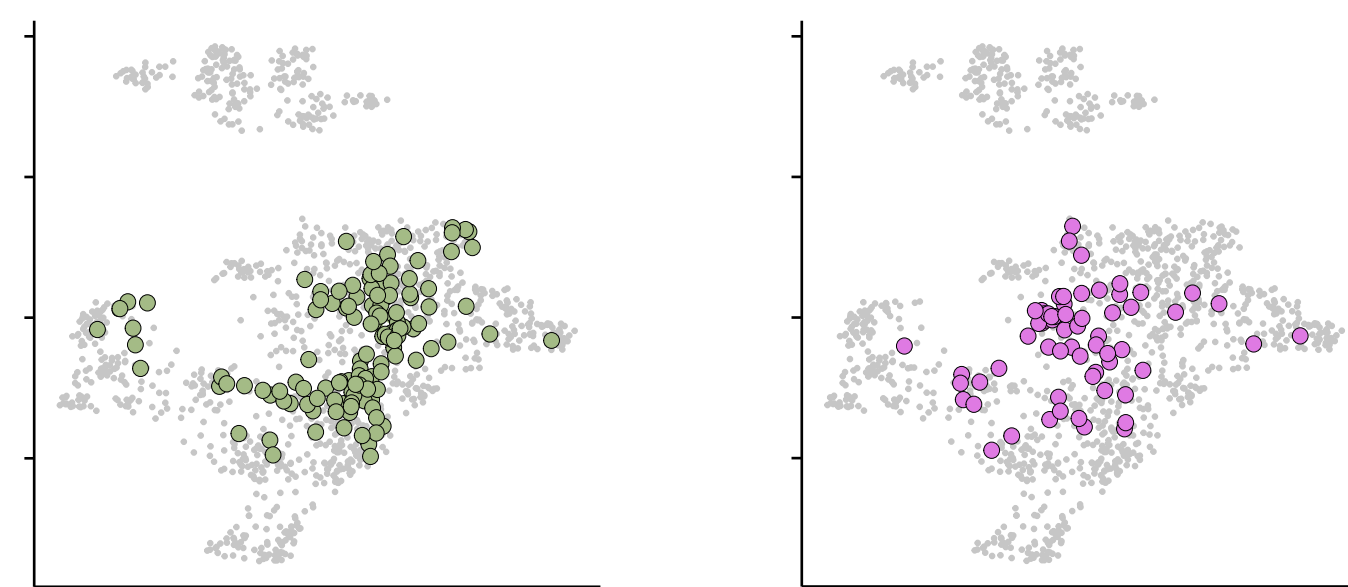
Melanoma lineage



Examples of metabolic heterogeneities within a cancer type

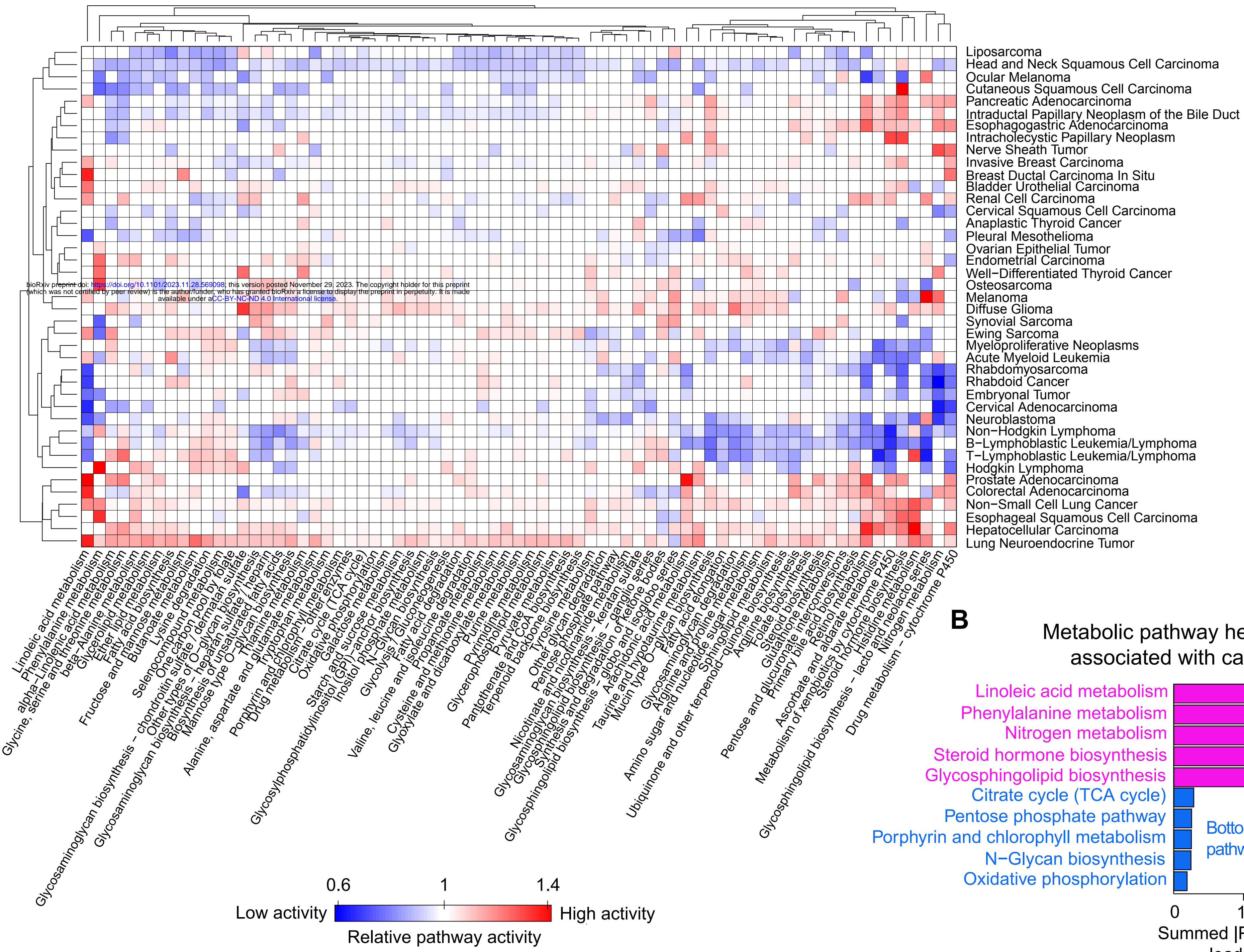
Non-Small Cell Lung Cancer

Ovarian Epithelial Tumor



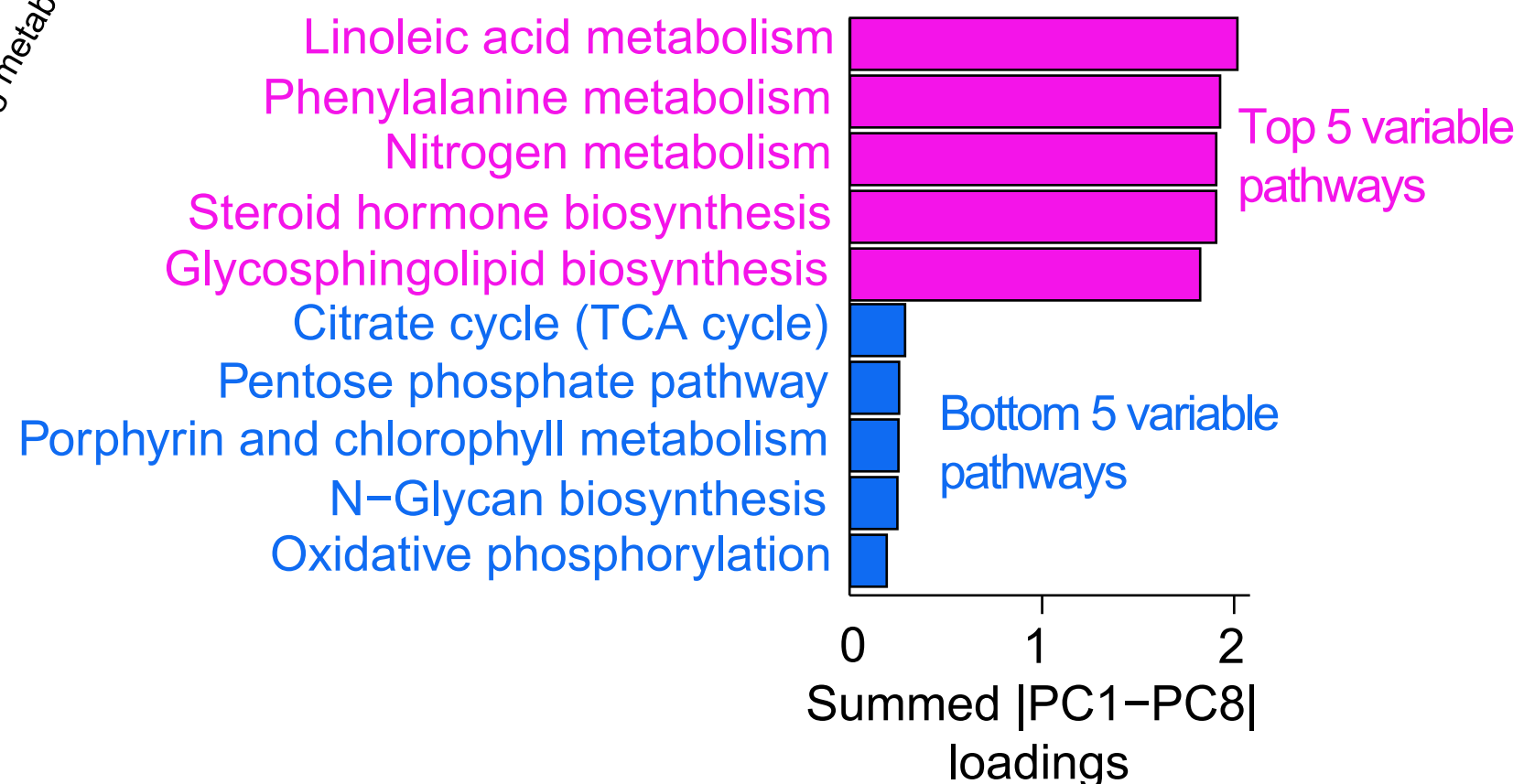
A

# Relative metabolic pathway activity across cancer types



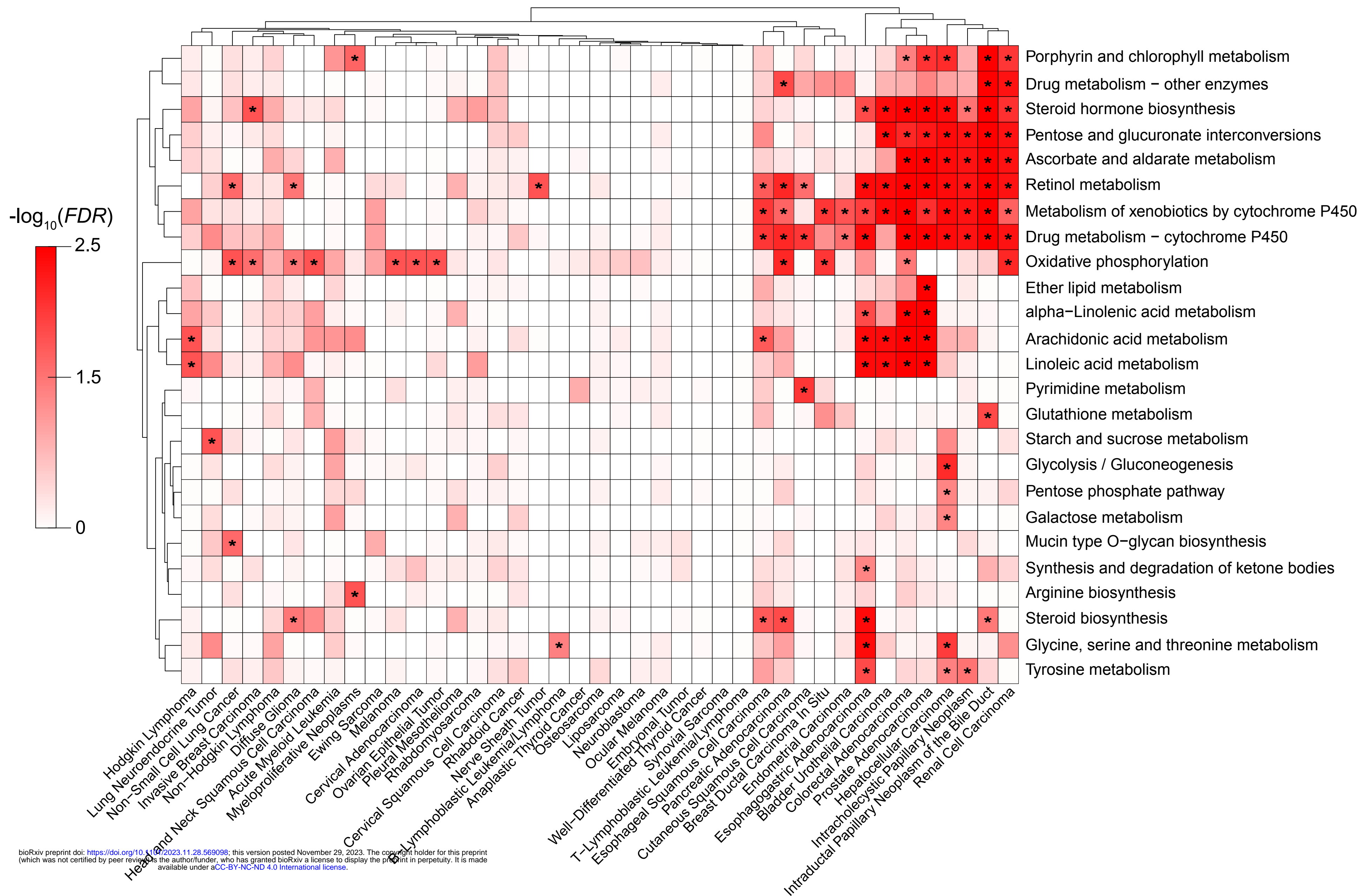
B

## Metabolic pathway heterogeneity associated with cancer type



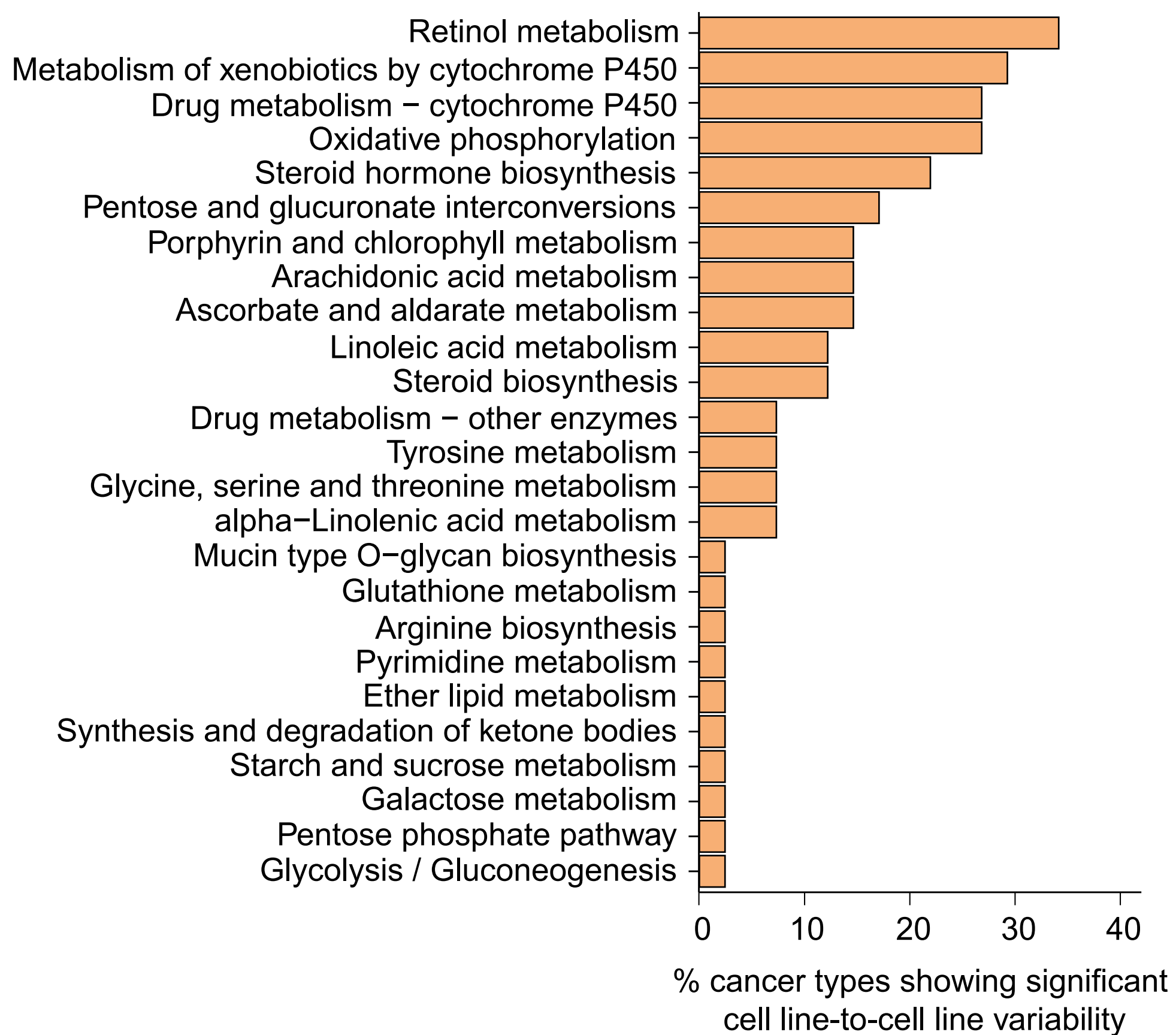
**A**

Cell line-to-cell line metabolic variability within each cancer type (\**FDR* ≤ 0.05)



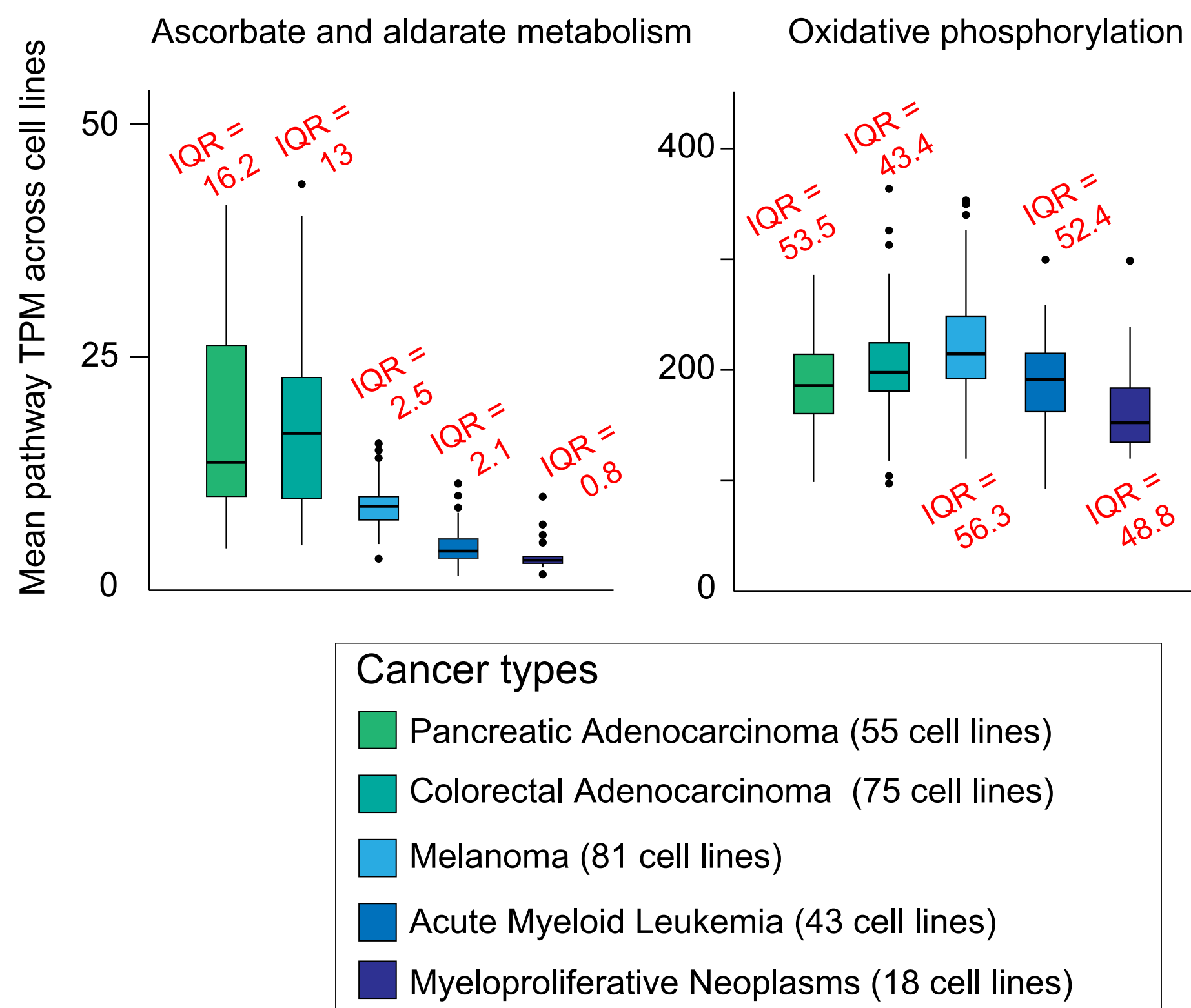
bioRxiv preprint doi: <https://doi.org/10.1101/2023.11.28.569098>; this version posted November 29, 2023. The copyright holder for this preprint (which was not certified by peer review) is the author/funder, who has granted bioRxiv a license to display the preprint in perpetuity. It is made available under aCC-BY-NC-ND 4.0 International license.

**B**



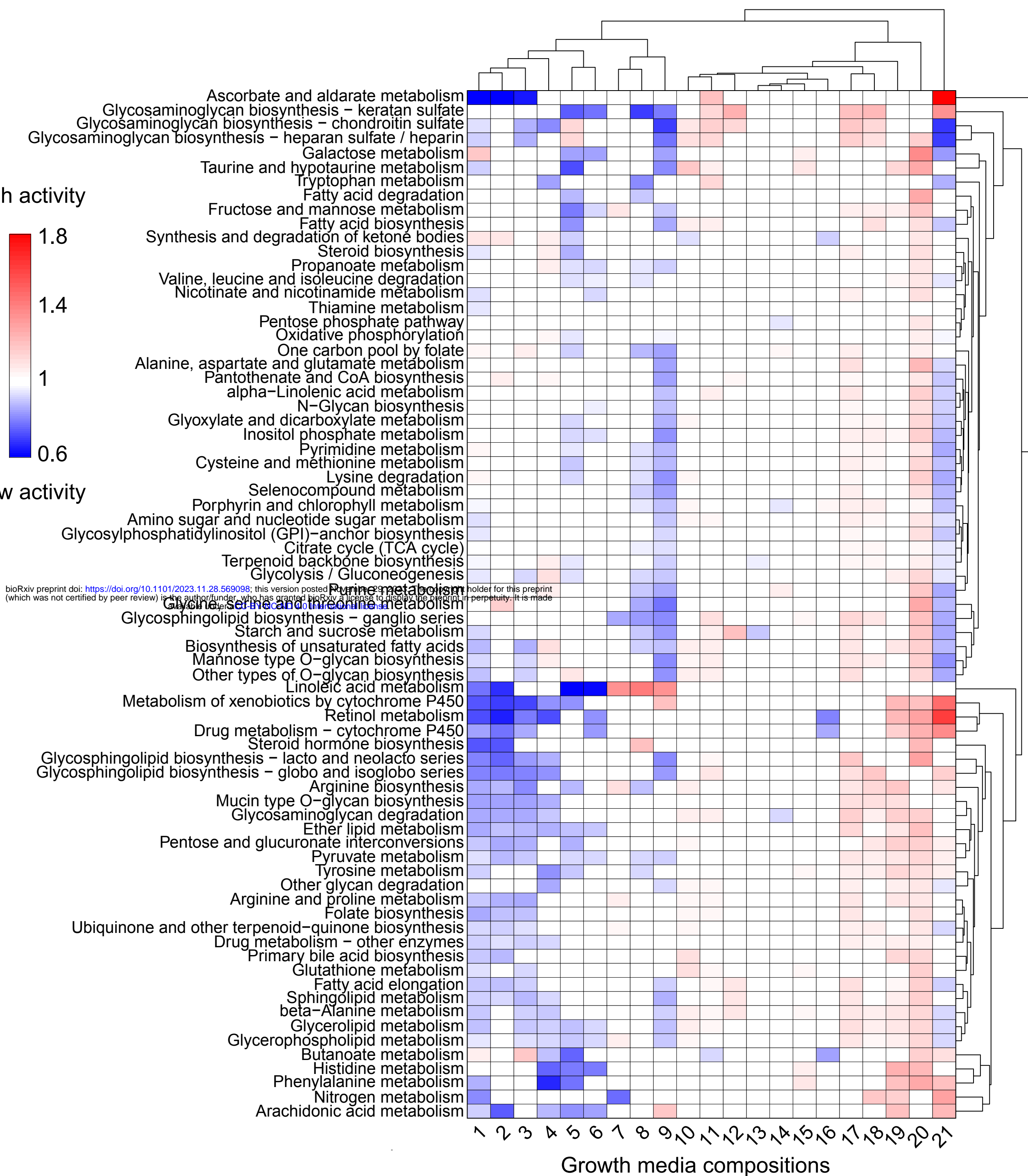
**C**

Distinct patterns of cell line-to-cell line variability in metabolic pathways across cancer types



A

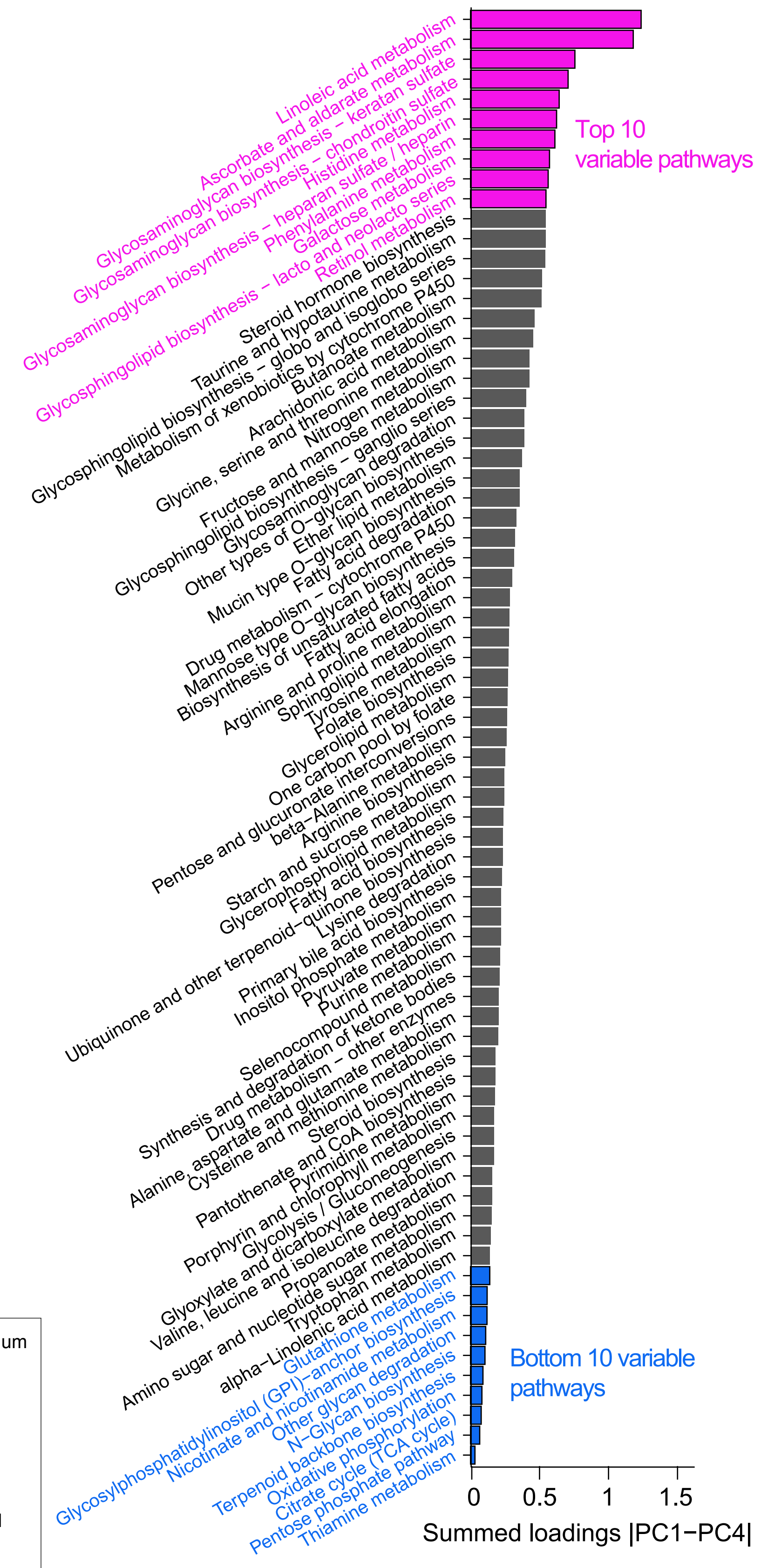
## Relative metabolic pathway activity across growth media



1: RPMI + 20% FBS    2: RPMI + 15% FBS    3: IMDM + 10% FBS    4: IMDM + 20% FBS + 4mM Glutamine + 1x Insulin-Transferrin-Selenium  
5: F12 + 15% FBS + 2mM Glutamine    6: EMEM + 10% FBS    7: L-15 + 10% FBS    8: EMEM + 10% FBS + 2mM Glutamine + 100µM NEAA  
9: IMDM + 10% FBS + 2mM Glutamine    10: MEM + 10% FBS    11: DMEM + 10% FBS    12: DMEM:F12 + 10% FBS    13: F12 + 10% FBS  
14: RPMI + 10% FBS + 2mM Glutamine    15: RPMI + 10% FBS    16: DMEM + 10% FBS + 2mM Glutamine    17: RPMI + 5% FBS  
18: McCoy's 5A + 10% FBS    19: RPMI + 10% FBS + 2mM Glutamine + 25mM HEPES + 25mM Sodium bicarbonate  
20: DMEM:F12 + 5% FBS + 2mM Glutamine + 5µg/ml Insulin + 10µg/ml Transferrin + 30nM Selenium + 10nM Hydrocortisone + 10nM Beta estradiol  
21: OPAC:Ad+++ (1:1)

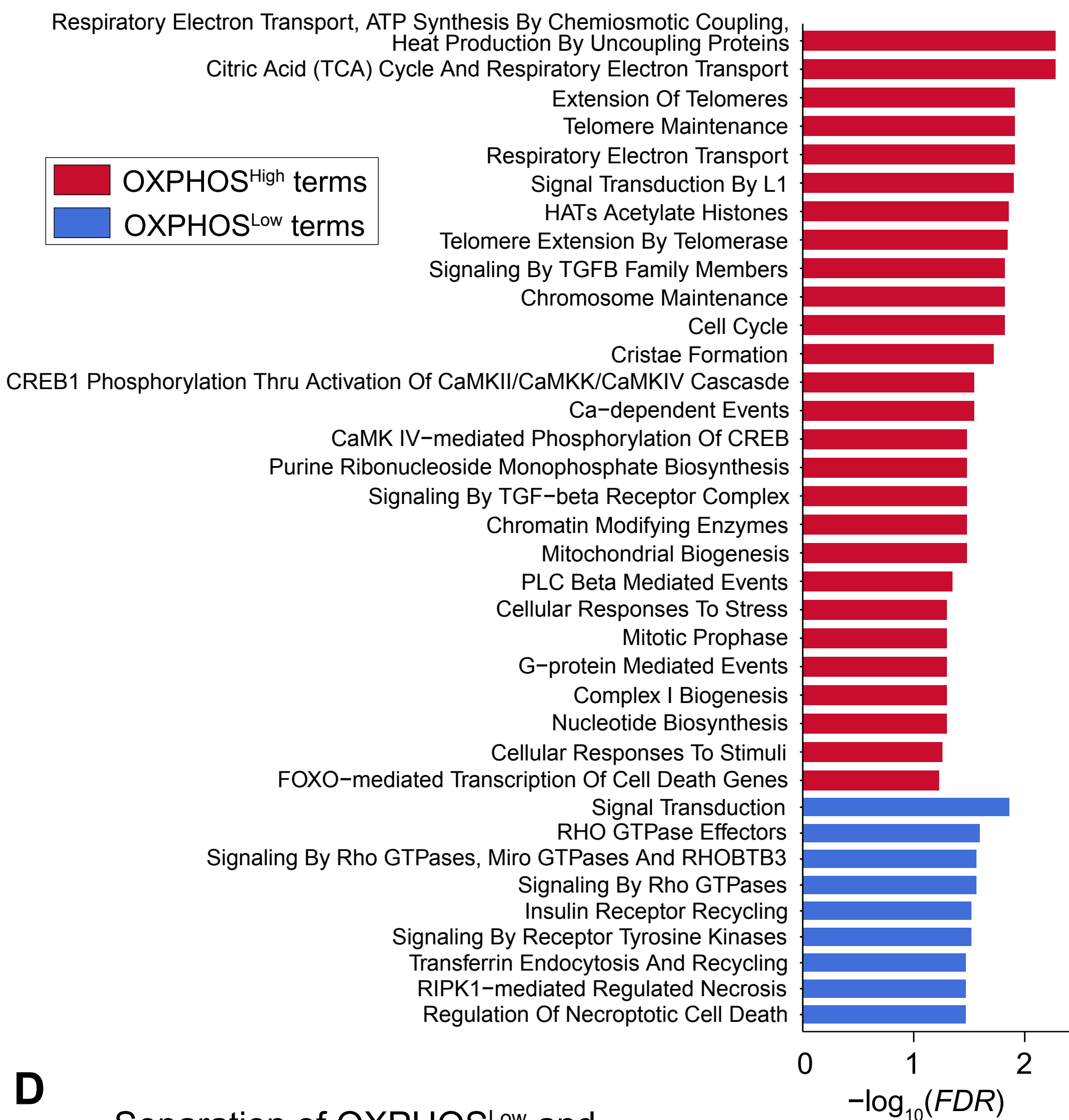
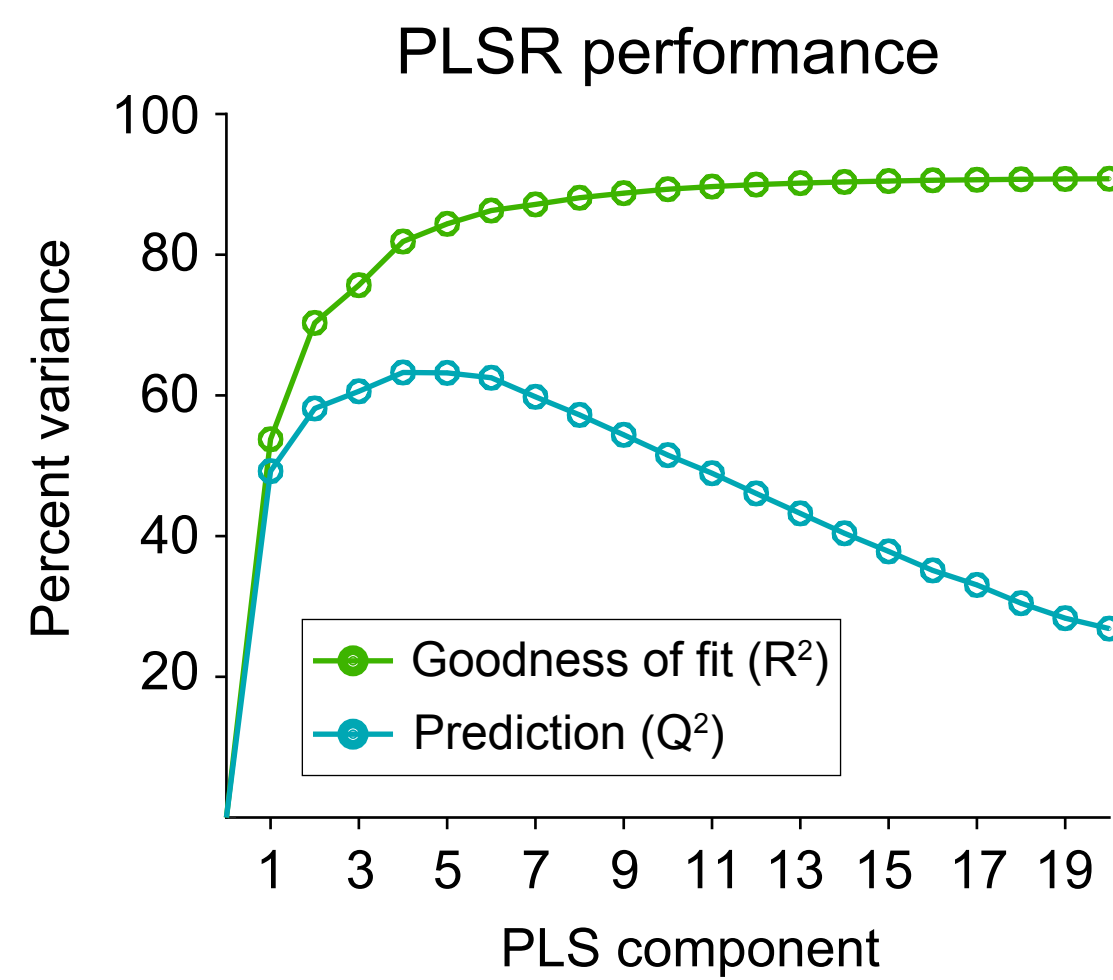
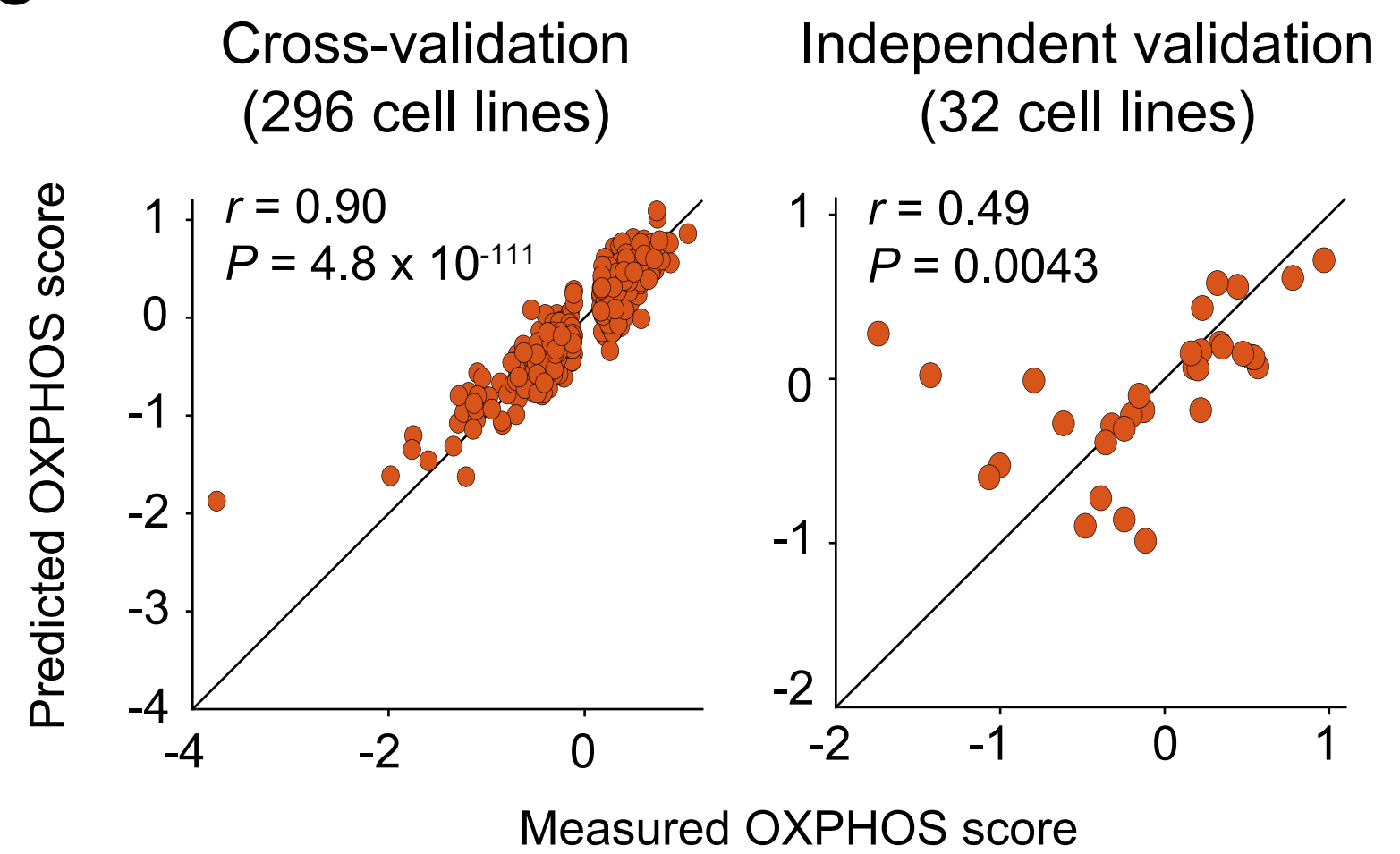
B

## Metabolic pathway heterogeneity associated with growth media



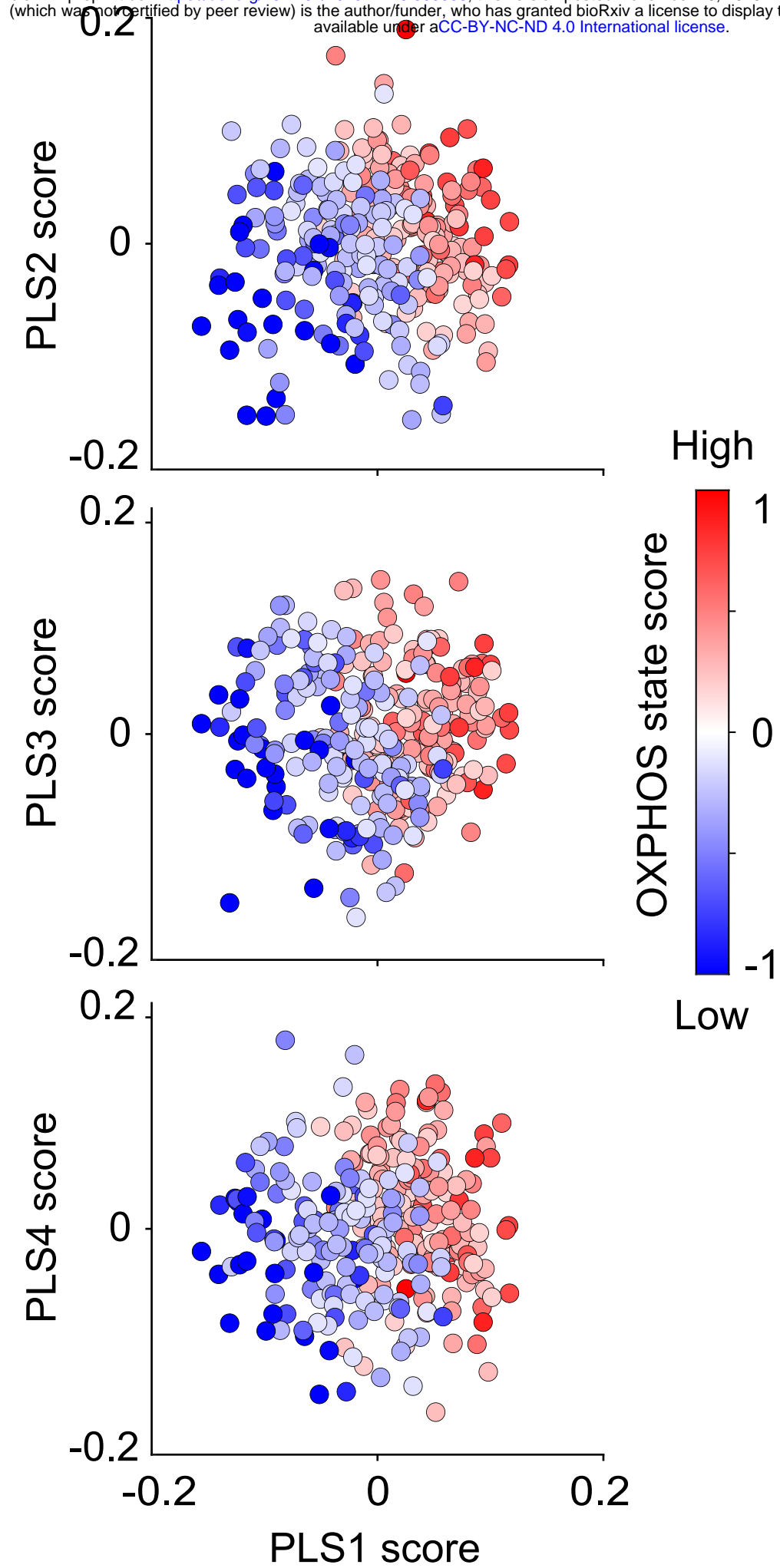
**A**

### Pathway enrichment of OXPPOS state-specific vulnerabilities ( $FDR \leq 0.05$ )

**B****C****D**

### Separation of OXPPOS<sup>Low</sup> and OXPPOS<sup>High</sup> cell lines by PLS scores

bioRxiv preprint doi: <https://doi.org/10.1101/2023.11.28.569098>; this version posted November 29, 2023. The copyright holder for this preprint (which was not certified by peer review) is the author/funder, who has granted bioRxiv a license to display the preprint in perpetuity. It is made available under aCC-BY-NC-ND 4.0 International license.

**E**

### Significant OXPPOS state-specific gene vulnerabilities

